Relationship between stylolite morphology and the sealing potential of stylolite-bearing carbonate cap rocks

Jun Wu [a, b, c*], Tailiang Fan [a, b], Enrique Gomez-Rivas [c], Qian Cao [d], Anna Travé [c], Zhiqian Gao [a, b], Zhihong Kang [a*], Daniel Koehn [e], Paul D. Bons [f, g]

*E-mail addresses of the corresponding authors: *zgdzdxbjwj@126.com (J. Wu), kangzh98@cugb.edu.cn (Z. Kang)*

a, School of Energy Resources, China University of Geosciences (Beijing), Beijing 100083, China

b, Key Laboratory of Marine Reservoir Evolution and Hydrocarbon Enrichment Mechanism, Ministry of Education, Beijing 100083, China

c, Department of Mineralogy, Petrology and Applied Geology, Faculty of Earth Sciences, University of Barcelona (UB), Barcelona 08028, Spain

d, Exploration and Development Research Institute of PetroChina Changqing Oilfield Company, Xi'an 710018, China

e, Friedrich Alexander University (FAU) Erlangen Nüremberg, Geozentrum Nordbayern, Schlossgarten 5, 91054 Erlangen, Germany

f, Department of Geosciences, University of Tübingen, Wilhelmstr. 56, 72074, Tübingen, Germany

g, School of Earth Science and Resources, China University of Geosciences (Beijing), Beijing 100083, China

This is a postprint version of this article. For the copy-edited version please visit:

Wu, J., Fan, T., Gomez-Rivas, E., Travé, A., Gao, Z., Kang, Z., Koehn, D., and Bons, P.D. 2022. Relationship between stylolite morphology and the sealing potential of stylolite-bearing carbonate cap rocks. GSA Bulletin, doi: https://doi.org/10.1130/B36297.1.

DOI: https://doi.org/10.1130/B36297.1

Website: https://pubs.geoscienceworld.org/gsa/gsabulletin/article-abstract/135/3-4/689/614954/Relationship-between-stylolite-morphology-and-the

Relationship between stylolite morphology and the sealing potential of stylolite-bearing carbonate cap rocks

Jun Wu [a, b, c*], Tailiang Fan [a, b], Enrique Gomez-Rivas [c], Qian Cao [d], Anna Travé [c], Zhiqian Gao [a, b], Zhihong Kang [a*], Daniel Koehn [e], Paul D. Bons [f, g]

*E-mail addresses of the corresponding authors: *zgdzdxbjwj@126.com (J. Wu), kangzh98@cugb.edu.cn (Z. Kang)*

a, School of Energy Resources, China University of Geosciences (Beijing), Beijing 100083, China

b, Key Laboratory of Marine Reservoir Evolution and Hydrocarbon Enrichment Mechanism, Ministry of Education, Beijing 100083, China

c, Department of Mineralogy, Petrology and Applied Geology, Faculty of Earth Sciences, University of Barcelona (UB), Barcelona 08028, Spain

d, Exploration and Development Research Institute of PetroChina Changqing Oilfield Company, Xi'an 710018, China

e, Friedrich Alexander University (FAU) Erlangen Nüremberg, Geozentrum Nordbayern, Schlossgarten 5, 91054 Erlangen, Germany

f, Department of Geosciences, University of Tübingen, Wilhelmstr. 56, 72074, Tübingen, Germany

g, School of Earth Science and Resources, China University of Geosciences (Beijing), Beijing 100083, China

Abstract: The sealing effectiveness of cap rocks bearing different types of stylolites is analyzed using a combination of petrographic, petrophysical, pore structure and sealing capacity characterization techniques. This study is based on examples of carbonate cap rocks that seal ultradeep hydrocarbon reservoirs of the Tarim Basin (China). Samples from both drill cores and their outcrop analogues are investigated to quantify how morphology does influence the sealing capacity of different types of stylolite-bearing rocks. The study cap rocks consist of mudstone, wackestone to

packstone, grainstone and dolomitic limestone. Four types of stylolites are identified: rectangular layer, seismogram pinning, suture & sharp peak and simple-wave like types. The difference in the sealing capacity of carbonate cap rocks is attributed to their pore structure connection and the types of stylolites they develop. Samples bearing simple-wave like stylolites have the best sealing capacity, followed those with rectangular layer and suture & sharp peak types, whereas carbonates hosting seismogram pinning type have the lowest sealing capacity. The impact of stylolite segments on the rock sealing properties, however, differ from one segment to another. Rectangular layer type stylolites can be divided into three distinct segments (with good, moderate and poor sealing, respectively). Both the seismogram pining and suture & sharp peak stylolite types are divided in two parts, with the former one having moderate and poor sealing and the latter exhibiting good and moderate sealing. The simple wave-like type has a good sealing capacity all along the pressure-solution seam. The most effective sealing barriers for vertical fluid flow form when (1) calcite and siliceous cements are pervasively distributed in the vicinity of stylolites, forming highly cemented zones with lower porosity and permeability than their surrounding host rocks; (2) stylolites are enriched in insoluble residues; (3) rare microfractures and dissolution vugs are found along the stylolites. This work provides useful examples for the prediction of the sealing potential of stylolite-bearing carbonate rocks according to stylolite morphology in other geological settings.

Keywords: Carbonate cap rocks; Stylolite types; Pore structure; Sealing effectiveness; Tarim Basin.

1 Introduction

The sealing capcity of cap rocks is one of the key factors for hydrocarbon accumulation and preservation (Lü et al., 2017). In addition to conventional cap rocks, such as shales, mudstones, gypsum and salt rocks, “tight” carbonates can also serve as a special type of cap rock (Grunau, 1997) for oil and gas reservoirs (Yang and Liu, 1991; Alsharhan and Sadd, 2000; Aguilera, 2006; Tang et al., 2008; Liu and Lü, 2010; Tonnet et al., 2011; Ellis et al., 2013; Tang et al., 2013; Lan and Lü et al., 2014; Menke et al., 2014; Rashid et al., 2015; Ronchi and Cruciani, 2015; Paganoni et al., 2016; Zhou et al., 2019). The sealing capacity of carbonate cap rocks is strongly linked with the properties of their pore networks (Nakayama, 1999; Wu et al., 2019). However, predicting the sealing capacity of cap rocks based on subsurface data, such as drill core and well logs, is generally a very challenging task (Schlömer and Krooss, 1997; Klokov et al., 2017). This is because carbonate rocks are almost always inherently heterogeneous (Hollis et al., 2010), as a result of the combined effects of (1) lateral and vertical variations of depositional environments, which result in highly variable distributions of lithofacies, rock textures and primary porosity (Makhloufi et al., 2013; Wilson et al., 2020), (2) multi-stage diagenetic overprints resulting from processes like mechanical and chemical compaction, dissolution, cementation and

mineral replacement (Mehrabi et al., 2016; Janjuhah et al., 2018), and (3) rock deformation at various scales, which results in the formation of tectonic structures such as (micro-) fractures, faults, veins, and tectonic stylolites (Cazarin et al., 2019; Humphrey et al., 2019). Most studies of carbonate cap rocks have focused on identifying and establishing quantitative evaluation criteria of their sealing stability (Lü et al., 2017; Wu et al., 2018a), characterizing their pore structures (Wu et al., 2019a, 2021), and revealing how the depositional facies and the diagenetic evolution of the rock determine its sealing properties (Wu et al., 2018b; Lü et al., 2019; Wu, 2020).

Stylolites are often smooth to rough surfaces that form by chemical compaction. The driving force for compaction can either be either the overburden load or tectonic stresses. The two can be distinguished by the orientation of stylolites: parallel the bedding or in any other orientation, respectively (*e.g.*, Park and Schot, 1968; Laronne Ben-Itzhak et al., 2012; Rustichelli et al., 2015; Paganoni et al., 2016; Koehn et al., 2016; Beigi et al., 2017; Rashid et al., 2017; van der Voet et al., 2020). As an ubiquitous diagenetic product, bedding-parallel stylolites in carbonate successions are of importance for hydrocarbon seepage due to their possible influence on local and regional fluid flow in the subsurface (Bruna et al., 2013; Rustichelli et al., 2015; Gomez-Rivas et al., 2022). Moreover, they can be controls for mineralization and can be ultilized for basin analysis (Beaudoin et al., 2019). Research into their formation mechanisms and how they impact permeability has therefore significantly increased

over the past years (e.g., Heap et al., 2014; Mehrabi et al., 2016; Heap et al., 2018; Toussaint et al., 2018; Bruna et al., 2019 and references therein).

Compared with their host rocks, rock volumes that contain or are affected by stylolites typically show anomalous porosity and permeability (Laronne Ben-Itzhak et al., 2012; Rustichelli et al., 2015; Ehrenberg et al., 2016; Morad et al., 2019). On the one hand, stylolites can provide pathways for fluid flow parallel to them (Heap et al., 2014; Martín-Martín et al., 2018), and can thus act as conduits for the migration of dissolved materials and hydrocarbon (Ehrenberg et al., 2016; Ehrenberg and Wu, 2019; Liu et al., 2020a). On the other hand, stylolites can also act as barriers to stylolite-normal flow (Sassen and Moore, 1988; Leythaeuser et al., 1995; Mehrabi et al., 2016; Beigi et al., 2017; Bruna et al., 2019). Furthermore, stylolites can potentially translate their behaviour in the course of the geological history of a basin, acting as barriers or conduits at different times (e.g., Gomez-Rivas et al., 2015, 2022; Martín-Martín et al., 2018; Humphrey et al., 2019). In other cases cases, stylolites appear not to have influenced the rock permeability in any way (e.g., Heap et al., 2018). Accordingly, stylolitization can either have a positive, negative or neutral impact on the sealing quality of cap rocks.

Much progress has been made in the characterisation and classification of stylolites (Park and Schot, 1968; Railsback, 1993; Laronne Ben-Itzhak et al., 2014; Koehn et al., 2016) and on gaining insights into the issue of whether stylolites act as barriers or conduits for fluid flow (Alsharhan and Sadd, 2000; Marfil et al., 2005;

Heap et al., 2014; Mehrabi et al., 2016; Paganoni et al., 2016; Martín-Martín et al., 2018; Bruna et al., 2019; Humphrey et al., 2019). Koehn et al. (2016) pointed out that the stylolite morphology may influence the rock's sealing capacity but did not provide quantative petrophysical measurements. It is not yet fully clear how rock types determine stylolite development and what the controlling factors are on their sealing capacity and that of their host rocks (Ning et al., 2018). Resolving these questions and uncertainties is particularly relevant to better understand the evolution of carbonate cap rocks, such as those of the Tarim Basin that are analyzed with regard to rock types, cycles, and stylolite development in this study.

A good example of the sealing capacity of carbonate cap rocks is that of the oil and gas fields of the Tarim Basin (e.g., Qian et al., 2012). The Lower-Middle Ordovician Yingshan Formation carbonate strata of the Tarim Basin have become an important target for hydrocarbon exploration in the past two decades (He et al., 2016; Qi, 2016; Li et al., 2020). The characteristics of fractured-vuggy carbonate reservoirs within these strata fluctuates laterally and vertically due to multi-layered paleokarst systems (Tian et al., 2016). The carbonate cap rocks of the Tarim Basin in this study have poor continuity in a single layer, whereas multilayer carbonate cap rocks are vertically well-superimposed (Wu et al., 2018a; Wu, 2020). The local carbonate reservoirs are characterized by a combination of a fracture-cavity type reservoir and upper tight carbonate rock layers (Zhou et al., 2019). The tight carbonate units are regarded as cap rocks for ultra-deep carbonate petroleum reservoirs of the Tarim

Basin because they are the key factor in determining of a carbonate reservoir will contain oil and gas (He et al., 2016; Jiao, 2018; Cao et al., 2019) and therefore have significant economic importance (Qian et al., 2012; Lü et al., 2017, 2019). The availability of samples from drill core and outcrop analogues, as well as the existing knowledge of the sedimentology, diagenesis and petrographysical properties of these cap rocks makes it possible to systematically analyze the influence of stylolites on the rock's sealing capacity (Qian et al., 2012; Ning et al., 2018; Wu et al., 2018a, 2018b; Lü et al., 2019). We present an integrated study of stylolite types and investigate the quantitative influence of stylolites on the sealing capacity of the cap rocks in the Tarim Basin.

The main objectives of this study are to (1) characterize the dominant lithologic types and morphological features of stylolites, (2) unravel the petrophysical properties and pore structures of these stylolite-bearing cap rocks, and (3) study the relationship between stylolite types and the sealing capacity of carbonate cap rocks. This study not only helps to quantitatively evaluate the sealing features of the Penglaiba Formation in view of hydrocarbon exploration in the Tarim Basin, but also contributes towards a better understanding of the stylolite types and their roles in the sealing behavior of cap rocks in carbonate reservoirs worldwide.

2 Geological setting

The Tarim Basin is the largest petroliferous basin in the northwestern part of

China, and covers an area of 5.6×10^5 km^2 (Fig. 1A). The Tahe oilfield is located in the Tabei Uplift of this basin and it is bounded by the Luntai fault to the north, the Shuntuoguole uplift to the south, the Halahatang sag to the west, the Caohu depression to the east and the Manjiaer depression to the southeast. Four well-exposed outcrop sections that are studied in this contribution are located in Bachu and Keping Counties, along the cliff of the Keping uplift in the northwest region of the Tarim Basin (Fig. 1B).

2.1 Stratigraphy

The Lower-Middle Ordovician carbonate sequences consist of the Lower Ordovician Penglaiba, Lower-Middle Ordovician Yingshan and Middle Ordovician Yijianfang Formations (Fig. 2).

(1) The dominant lithology of the Penglaiba Formation is fine to medium crystalline dolomite, which was deposited in a carbonate platform with evaporation (Liu et al., 2020b).

(2) The Yingshan Formation is the target in this study and is divided in two parts by a third-order sequence boundary (Msb3) (Wang et al., 2019). The lower part of this formation is composed of dolostones and dolomitic limestones intercalated with peloidal grainstones that were deposited in the lagoon and tidal flat of a restricted platform (Wang et al., 2018). The upper part mainly comprises intraclastic grainstones, peloidal packstones and mudstones that are interpreted as a result of deposition of

intraplatform shoal and intershoal sea sediments in an open platform. The heterogeneous carbonate cap rocks are more evenly distributed in the upper part of this formation.

(3) The Yijianfang Formation is mainly composed of bioclastic grainstones, oolitic grainstones and reef framestones that were deposited in a platform margin reef and in shoal complexes (Wang et al., 2019).

2.2 Structural evolution

The burial history of the Ordovician carbonate strata in the Tahe oilfield shows that five orogenic events (Chen et al., 2014), including the Caledonian, Hercynian, Indosinian, Yanshanian and Himalayan orogenies took place in the Tahe oilfield, and all affected the burial and uplift evolution of the studied rocks (Fig. 3A). Significant uplift occurred during the Early Ordovician to the Middle Ordovician (Middle Caledonian orogeny), the late Devonian to early Carboniferous (Early Hercynian orogeny) and the late Permian (Late Hercynian orogeny). In particular, the Middle Caledonian and Early Hercynian orogenies caused extreme erosion of Ordovician strata in the northern Tahe oilfield, resulting in a direct contact between the Lower-Middle Ordovician Yingshan Formation and the Lower Carboniferous Bachu Formation (Yan et al., 2011). In contrast, the complete Ordovician sequence is preserved in the southern Tahe oilfield (Tian et al., 2016).

The burial history of the four study outcrops shows that after initial

sedimentation in the Early Ordovician, the Yingshan Formation deposits were subjected to progressive subsidence during the Late Carboniferous that brought them down to a depth of 2,400 m, followed by a relatively slow subsidence period during the Middle Permian (which continued burial down to 2,900 m) and, finally, a rapid subsidence event in the Late Permian that resulted in a peak burial depth of more than 4,000 m (Fig. 3B) (Du et al., 2016). Therefore, these carbonate cap rocks were intermediately to deeply buried during the Hercynian orogeny. After the rapid subsidence an uplift event occurred at the beginning of the Triassic followed by several subsidence and uplift episodes until the present day (Dong et al., 2013).

Diagenetic phases of carbonate rocks of the Yingshan Formation from subsurfaces and outcrop analogues are characterized by mechanical and chemical compaction, cementation, dissolution, dolomitization, and micritization (Niu et al., 2010). The timing of each diagenetic process is shown in Figure 3. In terms of subsurface studies of cap rocks in the Tahe oilfield, the diagenetic processes can be broadly divided into three stages: penecontemporaneous to eogenetic to early mesogenetic, epigenetic, and early to late mesogenetic (Chen et al., 2003; Wu et al., 2018b). Three diagenetic stages were recognized in outcrop analogues of equivalent rocks comprising penecontemporaneous, shallow to intermediate burial, intermediate to deep burial, and an epigenetic stage (Dong et al., 2013; Du et al., 2016; Wu et al., 2021).

3 Samples and methods

This study is based on samples from the Yingshan Formation carbonate cap rock from outcrops located at the northwest margin of the Tarim Basin and vertical drill core from the Tahe oilfield of this basin. The significance of comparing rocks from outcrop analogues with those from drill cores can be summarized in three aspects: (1) drill core samples are considered representative of the rock sealing properties in the subsurface. However, it is always useful to compare their textures, diagenetic history and petrophysical properties with the same rocks found at the Earth's surface in outcrops; (2) Drill core studies are limited to 1D sampling, and often the studied rock volume does not fully represent the whole unit in the subsurface due to lateral changes and the small volume of the sample compared with that of the unit. The study of outcrop analogues allows the systematic study of the same samples in 3D, visualizing lateral facies changes and sedimentary structures and allowing a more representative sampling; (3) Most studies are based on outcrop analogues, including our own previous studies in the field area (Wu et al., 2018a, 2018b, 2019 and 2021), offer additional possibilities for data comparison. The field outcrops consist of four sections: Penglaiba (PLB), Kepingshuinichang (KPSNC), Yangjikan (YJK), and Dabantage (DBTG) outcrops (Fig. 1B). The drill core data from the Tahe oilfield were collected from nine wells: AD11, AD29, S88, S108-1, S115-1, T740, T760, TS3, and TS301 (Fig. 1C).

In order to minimize damage to the rocks during the sampling process, two steps were taken in the field: (1) the weathered carbonate layer on the outcrop surface was removed to expose the fresh rock surface; (2) the rock was then drilled to a depth of 0.4-0.5 m using a Shaw single backpack drill rig to obtain a cylindrical rock sample. During the sampling process, the drill cores were oriented vertically to ensure that stylolites from different cores are parallel to each other. Here we focus on carbonate rock samples with bedding-parallel (*i.e.*, sedimentary or diagenetic) stylolites. Sub-vertical stylolites of tectonic origin are rarely found in the Tahe oilfield and Keping Uplift. Hence, the impact of tectonic stylolites on fluid flow and permeability, and thus on the rock sealing capacity, is negligible.

The classification of carbonate rocks in this study is based on depositional textures (Dunham, 1962). The study of stylolites is carried out through a combination of visual analysis of samples from outcrops and drill cores, petrographic observations with optical and electronic microscopy, porosity and permeability tests and a combination of mercury intrusion capillary pressure and nitrogen gas adsorption analyses to characterize the distribution of the pore space in stylolite-bearing samples.

The pore size distribution scheme of carbonate cap rocks used here is based on the study of Wu et al. (2019) that classifies the pore space of carbonate cap rocks in macropore-I (>2.5 μm), macropore-II (1-2.5 μm), mesopore-I (0.25-1 μm), mesopore-II (0.1-0.25 μm), transitional pore-I (0.05-0.1 μm), transitional pore-II (0.01-0.05 μm), and micropore (<0.01 μm).

3.1 Visual analysis of stylolites

We adopted the stylolite classification scheme proposed by Koehn et al. (2016), which is based on the morphology and variations in amplitude of stylolite teeth. According to this classification scheme each category has a different potential sealing capacity. The density, amplitude and spacing of stylolites from drill core and outcrop plugs were measured in two dimensions using the methods proposed by Humphrey et al. (2019, 2020).

(1) Stylolite density (V) (in m^{-1}) is defined as the number of stylolites per meter of core, and was determined from multiple sections (photographs) within a core box, calculated by dividing the sum of bedding-parallel stylolites with the core length, and weighted per interval using equation (1):

$$V = \sum w_p \times v_p \quad (1)$$

where V is the stylolite density per core box, w_p is the proportion of measurable rock section inside the core box divided by the total length of measurable rock within the core box and v_p is the proportion of stylolites per measurable section of rock.

(2) Stylolite amplitude is determined by measuring the distance between the bottom and top of teeth in the middle of the core. Due to limited image resolution, only those stylolites were measured that are laterally continuous in an image and have an amplitude of at least ten pixels.

(3) Stylolite spacing between bedding-parallel stylolites was determined by

measuring the distance between the average mid-plane of two adjacent stylolites from the photos of each drill core. When stylolites are tilted more than 10°, the Terzaghi correction method (Terzaghi, 1965) was used to obtain the true spacing.

In addition, the relative timing of the formation of diagenetic products of the host rocks, and their structures, such as vugs and fracture veins, was determined through the identification of their cross-cutting relationships in core photographs and thin section photomicrographs, as was done by Humphrey et al. (2019).

3.2 Optical and electronic microscope petrography

A total of 125 cap rock samples from stylolite-bearing zones were chosen for thin-section analysis. Of these samples, 46 are from the four outcrop sections and 79 from drill cores (Fig. 1). Thin sections were selected with the aim of being representative of samples with abundant bedding-parallel stylolites with different morphologies, lithological types and from different carbonate cap rock intervals. All these thin-sections were 1/3-stained with Alizarin Red S to distinguish calcite and dolomite, and were impregnated with methylene blue dye to reveal the pore types. They were studied with an optical microscope. Cathodoluminescence (CL) emission analysis was conducted on polished thin sections to analyse diagenetic features under working conditions of 9.3 kV and 290 μA.

Fifteen carbonate rock samples (0.5 cm×1.0 cm×0.2 mm) coated with gold were investigated using an FEI Quanta FEG450 SEM instrument with a working current set

at an accelerating voltage of 20.0 kV and distance of 8-9 mm. Scanning electron microscopy (SEM) was used to characterize the micropore and cement morphology in cap rock intervals. In addition, energy dispersive spectrometer (EDS) was also used to measure mineral compositions of grains and cement.

3.3 Porosity and permeability tests

In order to quantify the porosity and permeability of stylolite-bearing carbonate cap rocks, 45 plug samples with a diameter of 25 mm were selected from four outcrops and six wells. The porosity and permeability tests were carried out following Chinese standard industry methods (GB/T 29172-2012, 2013). The instrumental error for the porosity and permeability analyses was ± 0.1‰. A QK-98 Helium Gas porosimeter was used for the porosity measurements of these samples, and permeability tests were performed with a GDS-90F Helium Gas Permeameter under applied test pressures ranging from 0.689 to 2.76 MPa. The detailed handing processes include four steps: (1) The plug samples were cleaned and dried. (2) The helium porosities of all samples were calculated from the difference between measured rock bulk density and skeletal density using the helium expansion method (see Wang and Yu (2017) for details of the procedure). (3) The permeabilities of these samples were tested under a constant pressure gradient using a bubble flowmeter to allow helium to pass through the cylindrical samples until the permeability value obtained was stable (Wu et al., 2021). (4) The permeabilities of all rock samples were

calculated using Darcy's law, and then corrected according to Klinkenberg's method (Zhang et al., 2021).

3.4 Combination of mercury intrusion capillary pressure and nitrogen gas adsorption analyses

Sixteen carbonate cap rock plugs (25 mm in diameter and 34-42 mm in length) were selected to investigate their sealing behavior using an Autopore IV9520 Micropore Structure Analyzer. The sealing performance of these rock samples was determined. The detailed description of the combination of mercury intrusion capillary pressure (MICP) and nitrogen gas adsorption (N_2GA) test methods can be found in Wu et al. (2019, 2021). The capacity of sealing oil and natural gas of the carbonate cap rock can be expressed by the cover coefficient (*CC*) in specific traps (Cheng et al., 2006). A high cover coefficient (*CC*) value expresses a good sealing performance of cap rock to oil and natural gas, and vice versa.

In order to quantitatively characterize the impact of each stylolite type on the cap rock sealing potential, three steps were taken: (1) both the number of individual stylolites of each type and the total number of all stylolites were counted on the outer cylindrical surface of samples. However, some stylolites are not easy to be counted due to their poor continuity or low amplitude. In order to acount for all stylolites, thin sections of small-scale stylolites were used as a supplement to improve the statistical accuracy; (2) the proportion (P_i) of each stylolite type in *i*-th sample was determined

by dividing their number by the total number of four stylolite types; (3) the average cover coefficient ($CC_{avg.}$) of each stylolite type for multiple samples was calculated by the combination of the cover coefficient (CC) characterizing the whole sealing capacity and the weighted proportion of the specific stylolite types.

$$CC_{\text{avg.}j} = \frac{\sum_{i=1}^{n} P_i \times CC_i}{\sum_{i=1}^{n} P_i} \quad (2)$$

Where j is the index number of stylolite type (from 1 to 4, 1 is the rectangular layer type, 2 is the seismogram pinning, 3 is the suture & sharp peak type and 4 is the simple-wave like type), i is the index number of the sample that contains the type j-th stylolites. $CC_{\text{avg},j}$ is average cover coefficient of stylolite type j for multiple rock samples, CC_i is cover coefficient of the individual rock samples tested by the combination of mercury intrusion capillary pressure and nitrogen gas adsorption in the laboratory, P_i is the proportion of the number of this stylolite type to the number of total stylolites accounted in an individual sample, $\sum_{i=1}^{n} P_i$ is the sum of the proportions of stylolite of sample i (1 to n, with n being the total sample number of carbonate cap rocks that contain type j-th stylolites).

For instance, there are only two samples (DBTG-P10 (i=1) and SNC-E28 (i=2)) that contain the rectangular layer type (j=1) (Table 2), so we can get a value of n=2 when calculating the average cover coefficients of these stylolite-bearing carbonate cap rocks ($CC_{avg.1}$). Therefore, the $CC_{avg.1}$ can be calculated with equation (2):

$$CC_{\text{avg.1}} = \frac{\sum_{i=1}^{2} P_i \times CC_i}{\sum_{i=1}^{2} P_i} = \frac{P_1 \times CC_1 + P_2 \times CC_2}{P_1 + P_1} = \frac{0.12 \times 5.40 + 0.35 \times 4.17}{0.12 + 0.35} = 4.48 \quad (3)$$

3.5 High-pressure mercury intrusion porosimetry (HPMIP) analysis

A total of thirteen carbonate cap rock samples were selected to analyze pore structures. An Automatic 9510-III High-pressure Mercury Intrusion Porosimeter was utilized to obtain the pore size distribution according to the Chinese Oil and Gas Industry standard (GB/T 29171-2012, 2012). The experiment temperature and humidity are 20℃ and 44-54%, respectively. The test pressures range from 0.012 to 116.667 MPa, which corresponds to a pore radius ranging from 63 to 0.006 μm. As an important parameter to characterize the pore structure of rocks, the threshold pressure is the minimum capillary pressure where the non-wetting fluid phase begins to continuously enter the largest pore of a rock sample. In addition, the cumulative permeability contribution value refers to the percentage of permeability that can be provided at the specified pore throat radius and above.

4 Results

4.1 Lithologic types

Thin section observations reveal that mudstone, wackestone to packstone, grainstone and dolomitic limestone (corresponding to crystalline carbonate according

to Dunham's scheme) are the main lithologic types in the stylolite-bearing samples obtained from outcrops and drill core (Fig. 4). Wackestone to packstone is the dominant type for outcrop samples, accounting for 43.5% of the total rocks, followed by grainstone (34.8%) and mudstone (15.2%) (Table 1). In the drill core samples, wackestone to packstone and mudstone present the same relative proportion (38%), followed by grainstone (20.2%). Dolomitic limestone is the least abundant lithology, both in outcrop and drill core (6.5% and 3.8%, respectively). Here we describe the main lithologic types in detail.

4.1.1 Mudstone

Mudstone is predominately composed of a homogeneous micrite matrix, with a volumetric content ranging from 95.3% to 98.2% (average 96.9%) (Fig. 5A). The micrite crystals are generally less than 10 μm in size, and formed in a quiet, low-energy hydrodynamic depositional environment that corresponds to the intershoal sea of an open carbonate intraplatform. Mudstones are quite tight with only partial dissolution vugs and elongate microfractures that have been cemented by calcite crystals. In addition, fenestrae pores with diameters varying from 0.17 to 0.36 mm are completely filled with calcite cement. The calcite cements account for 3.1% (varying from 1.8% to 4.7%) of the rock volume.

4.1.2 Wackestone to packstone

Wackestone is composed of abundant micrite and minor peloids and bioclast

fragments, with an average volume percentage of 77.5%, 12.6% and 9.9%, respectively (Fig. 5B). Partially shattered subangular bioclast fragments are characterized by moderate sorting and their sizes range from 0.13 to 1.72 mm. The primary intragranular pores have almost disappeared due to intense mechanical compaction. Packstone is characterized by poor compaction. It is relatively well cemented and predominately contains abundant well-sorted peloids and moderately sorted intraclasts (Fig. 5C). The average total volumes of peloids and intraclasts are 42.5% and 34.6% of the rock, respectively. The intraclasts are 0.35-1.45 mm in size and they are dispersed in the rock.

4.1.3 Grainstone

Peloidal and intraclastic grainstone (Fig, 5D, E) both widely range in volume, varying from 34.5% to 68.4% and from 34.6% to 75.3%, respectively. Masses of peloids with oval to spherical shapes and with sizes varying from 0.23 to 4.25 mm are the primary components of these grainstones. Intraclasts show poor sorting with diameters varying from 0.18 to 2.6 mm and are embedded in sparry calcite. These grains are closely compacted or highly cemented and appear in a linear, stitched, concave-convex and curved contact. A vast majority of the intergranular pores, which show triangular and serrated shape with poor connectivity, are either completely cemented with calcite crystals or partially filled with pyrobitumen.

4.1.4 Dolomitic limestone

Subhedral and anhedral dolomite crystals range from 0.08 to 1.2 mm in size. The total volume of dolomite crystals varies from 35.6% to 49.3% of the rock. These dolomite crystals are concentrated along or in the vicinity of stylolites throughout the mictite matrix. Intercrystalline pores are rarely observed. Minor quantities of calcite cements are visible away from dolomite crystals (Fig. 5F).

4.2 Stylolite characterization

4.2.1 Occurrence of stylolites in cap rocks

Statistical analysis of stylolite types within the studied carbonate cap rock intervals (Figs. 6, 7) show that simple wave-like type stylolites are the most abundant stylolite type, accounting for almost 45% of the studied stylolites (Figs. 6A, 7D). In some cases, stylolites are arranged in anastomosing networks that formed during progressive chemical compaction. Seismogram pinning type stylolites are the second most abundant stylolite type, representing 23.5% of the total stylolites that were quantified (Figs. 6A, 7B). Suture & sharp peak type stylolites are the third most abundant type, representing 20.6% of the whole stylolite population (Figs. 6A, 7C). Rectangular layer type stylolites are the least abundant type and only constitute 11.8% of the total number of observed stylolites (Figs. 6A, 7A).

The stylolite density varies by more than an order of magnitude, ranging from

4.5 to 80/m with an average of 44.7/m (Fig. 6B). The dominant interval of stylolite density distributes in the range of 30-44/m, followed by the interval with a density in the range of 60–70/m. Proportionately, a stylolite density of less than than 10/m is of low abundance, accounting for 0.9% of the total samples. In terms of the comparison of stylolite density between rock types, the wackestone to packstone have the highest average stylolite density (45.8/m), followed by mudstone and peloidal and intraclastic grainstone with an average stylolite densities of 38.5/m and 31.2/m respectively, and dolomitic limestone which has the lowest average stylolite density (12.3/m).

The amplitude of individual stylolites shows a wide range of 0.1–4.5 cm (Fig. 6C). 25.6% of the measured stylolites have an amplitude in the range of 0.25–0.5 cm. and 21.4% in the range of 1.5–2.0 cm. In terms of the amplitudes of the four stylolite types, the rectangular layer type stylolites have the largest amplitudes (with an average of 2.2 cm) and these are widely distributed along the lithologic boundaries between peloidal grainstone and mudstone (Fig. 7A). Seismogram pinning type stylolites exhibit the second highest amplitude on teeth or spikes with an irregular geometry (average 2.0 cm). Suture & sharp peak type stylolites exhibit various amplitudes (average 1.9 cm) (Fig. 7C). Simple wave-like type stylolites are characterized by the lowest amplitudes (average 0.4 cm).

The spacing between consecutive stylolites ranges up to 32 cm and shows an approximately log-normal frequency distribution (Fig. 6D), with 50% of all spacings falling within the 0.5-2 cm range. No systematics could be observed in the

relationship between spacing patterns and lithology or stylolite type, except that, of course, smaller spacings correlate with higher stylolite densities.

4.2.2 Stylolitization-related products

(1) Calcite: this is the main mineral cementing the cap rock samples. It is an indicator of the relative timing between each calcite cement generation with respect to stylolite formation. Optical and cathodoluminescence microscopy, isotope geochemistry and fluid inclusion studies (Du et al., 2016; Shang, 2019) showed that blocky calcite cements derive from the dissolution process associated with stylolite formation, and that they fill microfractures and vugs, and also precipitated on the flanks of stylolite teeth of rectangular layer type stylolites (Figs. 7A, E, 8A). Seismogram pinning type stylolites bound calcitised dolomite and are cut by calcite veins (Fig. 7B). A comparison of fracture fillings between cap rock intervals and reservoir intervals shows that fractures are always completely filled with calcite cements in the cap rock intervals, but still be open or only partially filled in the reservoir intervals (Fig. 4). Completely-filled microfractures that are cut by simple wave-like type stylolites are oriented perpendicular or sub-perpendicular to the lateral direction of stylolites. Both unconnected and interconnected stylolite networks can be found locally. As measurements are collected from core photographs, the connection of stylolites could only be observed in 2D, and therefore cannot be considered fully representative of the 3D distribution of stylolite connection. Mirofractures show

complex cross-cutting relationships, with some microfractures now partially or completely filled to form veins. Typically, thin calcite veins are always cut by wider calcite veins (Fig. 7H).

(2) Dolomite: Euhedral/subhedral dolomite crystals are found within suture & sharp peak type stylolites (Fig. 8B, D). Some partially-open microfractures filled with dolomite crystals are observed in the proximity of stylolites. Additionally, these dolomite crystals are frequently coated by pyrobitumen (Fig. 8B). However, some euhedral dolomite crystals are found scattered in host calcitic rocks (Fig. 8C). Light grey calcitised dolomite was found between two stylolites in dark grey peloidal/intraclastic packstone (Fig. 7B). Furthermore, Han et al. (2013) revealed that the calcitised dolomite has $\delta^{13}C$ from -1.23‰ to +0.60‰ VPDB (average -0.14‰) and $\delta^{18}O$ from -8.87‰ to -4.96‰ VPDB (average -7.68‰), and the packstone is characterized by $\delta^{13}C$ composition ranging from –0.94‰ to -0.09‰ VPDB (average -0.64‰) and $\delta^{18}O$ signature ranging from –8.71‰ to -5.47‰ VPDB (average -6.56‰).

(3) Black bitumen, oxidized bitumen residue, and pyrite represent insoluble materials accumulated in less than 1.2 mm thick seams and occur in various amounts in different rock types from mudstone to grainstone. Black bitumen is frequently encountered in all four types of stylolites (Fig. 8A). It is typically concentrated along the crest and/or trough of rectangular layer type stylolites (Fig. 7A), but is rarely encountered in the flanks of teeth (Fig. 7F). Oxidized bitumen residue and

dissolution-enlarged porosity are found along the pressure-solution interfaces (Fig. 8F). Pyrite, ranging from 0.5% to 1.8% in volume content, is scattered along simple wave-like stylolites within peloidal and intraclastic grainstone and mudstone. Discrete euhedral pyrites (up to 0.25 mm in size) are embedded in the pyrobitumen along stylolites (Fig. 8E).

(4) Authigenic minerals: including goethite, halite, kaolinite, quartz and siliceous mass. Clustered goethite grew at the grain boundaries and the orientation of the crystals is perpendicular to microfacture walls (Fig. 9A). It is occasionly found along suture & sharp peak and simple wave-like stylolites in peloidal/intraclastic packstone and grainstone. Halite is present in the flanks of teeth of seismogram pinning stylolites and can sometimes be found in intergranular pores of host rocks, especially in peloidal and intraclastic grainstone (Fig. 9B). Clay minerals are clearly visible at the top of spikes of seismogram pinning stylolites in peloidal and intraclastic grainstone (Fig. 7G). Quartz and kaolinite are present in various amounts in intercrystalline pores of mudstone and in residual intergranular pores of peloidal and intraclastic grainstone (Fig. 9C, D). In addition, siliceous bands terminate at the suture & sharp peak stylolites in wackestone to packstone (Fig. 7I), and amorphous siliceous mass terminates at the simple wave-like stylolites in mudstone.

4.3 Porosity and permeability

Porosity measured in cores of the carbonate cap rocks that contain

bedding-parallel stylolites ranges from 0.22% to 2.60%, with an average of 1.06%. Porosity histograms show a unimodal and an assymmetrical distribution with a peak between 0.5% and 1%. The number of analyzed samples with a porosity lower than 0.5% is equal to that within the range of 1-1.5% (Fig. 10A). The permeability of bedding-parallel stylolite-bearing cap rocks varies from 0.001 to 1.36 mD and displays a unimodal distribution with a peak at 0.001-0.01 mD. More than 70% of the carbonate cap rock samples have permeabilities lower than 0.01 mD (Fig. 10B). A cross-plot of porosity and permeability (Fig. 10C) shows that there is no correlation between the two with an extremely low coefficient of determination (R^2=0.087). Some rock samples are characterized by relatively low porosity and relatively high permeability and vice versa.

4.4 Sealing performance of cap rocks

The cover coefficients for stylolite-bearing carbonate cap rocks are presented in Table 2. A good sealing capacity of carbonate cap rocks to natural gas in specific traps can be defined by a high cover coefficient, and vice versa. Our results show that carbonate cap rocks have a narrow range of cover coefficients from 3.9% to 5.4% (average 4.5%). Combined with Eq. (2), the average cover coefficients (CC_{avg}) of cap rocks representing the four stylolite types were calculated and are shown in Fig. 10D. In terms of stylolite morphology, the cover coefficients of rectangular layer stylolite-bearing cap rocks range from 4.17% to 5.4% (average 4.79%), those

corresponding to seismogram pinning, suture & sharp peak, and simple wave-like stylolite-bearing carbonate cap rocks vary from 3.9% to 4.58% (average 4.31%), from 4.14% to 5.4% (average 4.44%), and from 3.9% to 5.4% (average 4.51%), respectively. Therefore, the cap rocks bearing the four types of stylolites feature various sealing effectiveness. Rock samples containing simple wave-like stylolites present the best sealing capacity, followed by rectangular layer type and suture & sharp peak type. The seismogram pinning stylolites-bearing cap rocks show the poorest sealing performance.

4.5 Pore structure from high-pressure mercury intrusion porosimetry (HPMIP) analysis

The pore structure of carbonate cap rocks containing the different types of stylolites can be divided into four categories based on the morphology of HPMIP curves and pore size distribution (Fig. 11).

(1) Cap rocks bearing rectangular layer stylolites exhibit a vertical trend at the initial stage, with a relatively high threshold pressure (1.5 MPa). The pore mercury saturation increases over a narrow pressure interval, with a relatively high maximum mercury saturation (21.72%) (Fig. 11A). There is a relatively gentle ascent of the mercury intrusion curve at the intermediate stage. In addition, the cumulative permeability contribution increases significantly from 1.3% to 100% in the pore throat

range 0.01-0.016 μm (Fig. 11B). Cap rocks are sufficiently low porous and permeable rock layers that seal the top of reservoirs and other geologic formations. Pore throat radii of this cap rock show a bimodal distribution, with an average of 0.108 μm. The larger pore throat radius is 0.4 μm, while the smaller one is 0.0063 μm (Fig. 11B).

(2) Cap rocks bearing seismogram pinning stylolites display a gentle trend from the initial stage to the intermediate stage of the whole mercury intrusion process, with an extremely low threshold pressure (0.01 MPa). Additionally, the maximum mercury saturation of this stylolite-bearing cap rock is 25.83%, which is 4.11% higher than that of the first type of stylolite-bearing rocks (Fig. 11C). It reflects a large volume of mercury entering the pore space during the increase of intrusion pressure, indicating that the rock sample predominately consists of large pores. The cumulative permeability contribution of pore size larger than 63 μm is 77.6%. The mercury intrusion process shows a steady increase to 94.2% in the pore range of 25-63 μm and a relatively slow increase to 99.6% in the pore size of 6.3-25 μm. The pore throat radii of this stylolite-bearing carbonate cap rock are characterized by a wide range of 0.1-63 μm, with an average of 14.7 μm (Fig. 11D).

(3) Carbonate cap rocks with suture & sharp peak stylolites have a relatively low threshold pressure (0.3 MPa) and exhibit intermediate mercury intrusion curves with a steep slope (Fig. 11E). The pore mercury saturation slowly increases over a wide pressure range. The maximum mercury saturation is the lowest among the four types

of stylolites (12.85%). There is a steep cumulative permeability contribution curve (from 24.4% to 97.3%), which corresponds to the pore size of 0.1-0.4 μm. The pore throat radii of cap rock containing this type of stylolite indicate a bimodal distribution with a smaller model in the range of 0.063-0.16 μm and a larger model in the range of 0.63-1.05 μm (Fig. 11F).

(4) Cap rocks with simple wave-like stylolites exhibit a vertical trend in the initial stage with a significantly high threshold pressure (20 MPa), which indicates that it is not easy for mercury to be injected into pore space. This vertical trend is followed by a relatively horizontal line with a gentle slope in the intermediate test stage, with a relatively low maximum mercury saturation (13.78%) (Fig. 11G). The cumulative permeability contribution shows a sharp increment from 1.7% to 91.1% in the pore throat range of 0.01-0.016 μm and a gentle rise from 91.1% to 100% in the pore throat range of 0.0063-0.01 μm (Fig. 11H).The pore throat radii show a considerably unimodal distribution and the main pore throat size ranges from 0.0063 to 0.016 μm, implying that microscopic pores are quite developed (Fig. 11H).

5 Discussion

5.1 Relationship between stylolite morphology and lithology

5.1.1 Abundance of different lithologies

Overall, wackestones to packstones form the dominant lithology types among the

studied stylolite-bearing carbonate cap rocks (Table 1), while dolomitic limestone just represents a small proportion of all studied samples. However, a comparison between outcrop sections and drill cores reveal a different proportion of peloidal and intraclastic grainstone and mudstone for the stylolitized carbonate cap rocks. Peloidal and intraclastic grainstone for outcrop samples presents a higher proportion than that for well samples (34.8% vs. 20.2%), while mudstone from outcrop sections presents a lower proportion than that from drill cores (15.2% vs. 38%). This result can be attributed to: (1) an underestimation of the total number of stylolites from drill core samples with respect to the better exposed outcrop samples. Drill core samples are cut into two halves and the statistical analysis of stylolite distributions are performed at these fresh vertical sections. Stylolite distributions may be underestimated due to the fact that sampling from drill cores is limited in three dimensions compared to outcrop surfaces; (2) partially different diagenetic paths for outcrop and subsurface rocks, which was revealed to play an important role in controlling the distribution of carbonate cap rocks and their petrophysical properties (Wu et al., 2018b). The carbonate cap rocks of the subsurface in the Tahe oilfield underwent two significant chemical compaction stages that correspond to penecontemporaneous to eogenetic to early mesogenetic and early to late mesogenetic diagenetic stages (Fig. 3A). The carbonate cap rocks from outcrops underwent only one significant chemical compaction stage that corresponds to intermediate to the deep burial diagenetic stage (Fig. 3B). The difference in the diagenetic pathway resulted in the difference in

abundance of sylolite types: stylolites of the seismogram pinning and suture & sharp peak types are common in outcrop samples, while stylolites of rectangular layer and simple wave like types are more abundant in the subsurface of the Tahe oilfield. In addition, the carbonate cap rocks in outcrop sections underwent intense weathering and dissolution during the epigenetic stage, which increased the difficulty of laterally tracing stylolites for mudstones.

5.1.2 Stylolite types versus lithology

Stylolites of the rectangular layer and seismogram pinning types are abundant in peloidal and intraclastic grainstones (Fig. 12A, B, Table 3). This is attributed to: (1) the more heterogeneous character of this lithology compared to the others (Wu et al., 2019, 2021) and (2) the fact that the Yingshan Formation carbonates underwent two stages of tectonic uplift and subsidence during the Middle Caledonian and Early Hercynian orogenies (Chen et al., 2014). The heterogeneity of limestone fabrics favors the formation of high-amplitude stylolites (Railsback, 1993; Mehrabi et al., 2016; Humphrey et al., 2020). The complex tectonic activity of the Yingshan Formation carbonates, including different phases of uplift and subsidence, contributed to the onset of multiple phases of pressure-solution and chemical compaction. As shown in Fig. 7C, younger stylolites cannibalize older ones, indicating that some stylolite surfaces could have been re-activated and new ones formed to form complex stylolite patterns that are difficult to be traced in the carbonate cap rock intervals. The

stylolite morphology is not easy to identify due to the masking of the original stylolite roughness. This phenomenon was also observed within the Middle Jurassic carbonate reservoirs from the Paris Basin (France) (Beaudoin et al., 2019).

Suture & sharp peak and simple wave-like stylolite types are both more abundant in wackestone to packstone. However, there is still some minor diversity among the two types of stylolites or within small layers. The suture & sharp peak type stylolites are approximately equally abundant in mudstone and peloidal and intraclastic grainstone (Fig. 12C), but simple wave-like type stylolites are more frequent in mudstone compared to peloidal and intraclastic grainstone (Fig. 12D).

Rectangular layer stylolites are more likely to develop along the transitional boundary of two lithologies, which can result in a higher amplitude because slower dissolving layers pin teeth resulting in linear amplitude growth as a function of compaction (Koehn et al., 2016). Paganoni et al. (2016) proposed that textural heterogeneity could facilitate the onset of stylolitization along specific discontinuity surfaces. Peloids/intraclasts in grainstone not only have larger grain sizes than micrites (refer to fine calcite crystals < 10 μm in diameter) in mudstone, but also larger amounts of insoluble materials within the stylolite surface. These grains display uneven dissolution, which contributed to the formation of large offsets and high-amplitude stylolites.

In contrast, simple wave-like type stylolites, which are characterized by low amplitudes, are always present in mudstone with a homogeneous micrite matrix.

Railsback (1993) concluded that relatively abundant undulatory surfaces are more likely to be distributed in matrix fabric-dominated carbonate rocks. By definition, micrite has smaller grain sizes than other carbonate components and shows a uniform sensitivity in terms of pressure-solution, thus resulting in the shortage of sufficient offsets along pressure solution surfaces. Therefore, once the dissolved materials diffuse through the homogeneous matrix, simple wave-like type stylolites will be pervasively formed in mudstone.

The four types of stylolites are rarely found in dolomitic limestone in this study. This is probably a consequence of (1) the higher solubility of calcite compared to dolomite, which favours stylolite formation in limestones (Zhang et al., 2002; Peacock and Azzam, 2006; Laronne Ben-Itzhak et al., 2014; Mehrabi et al., 2016; Martín-Martín et al., 2018), and because (2) dolomite crystals provide a strong framework that prevent chemical compaction during the burial stage. Smith (2000) suggested that dolomite crystals that concentrate along stylolite surfaces indicate that these stylolites once acted as preferred conduit for dolomitizing fluids. However, the scarcity of dolomite crystals along the stylolites in this study indirectly highlight the sealing behavior of stylolites during this fluid flow phase.

Relationships between stylolite types and lithology indicate that the stylolite morphology is dependent on the host rock heterogeneity and stylolite growth regime (Railsback, 1993; Koehn et al., 2016; Beaudoin et al., 2019; Humphrey et al., 2020). A close relationship exists between the magnitude of lithologic fabric contrast and the

stylolite amplitude (Shappard, 2002). Mud-supported carbonates (mudstones and wackestones) lack contrasts along pressure-dissolution surfaces that are sufficient to generate offsets, which this contributes to the abundant occurrence of low-amplitude stylolites (e.g., simple wave-like type). Grain-supported carbonates (packstones and grainstones) always show significantly variable sensitivity to pressure dissolution and these grains can probably be broken as offsets form, which contributes to the present of high amplitude stylolites (e.g., rectangular layer type).

5.2 Relationship between stylolite types and porosity and permeability

Overall, the porosity of stylolite-bearing carbonate cap rocks has no evident relationship with permeability (Fig. 10C). However, the cross-plots between porosity and permeability of rock samples containing the four types of stylolites exhibit high variability (Fig. 13, Table 3). There is a negative correlation between porosity and permeability with a higher coefficient of determination in cap rocks containing rectangular layer stylolite than those of rock samples containing suture & sharp peak stylolites (Fig. 13A, C). No positive correlation between the two parameters can be recognized for the seismogram pinning type stylolitic cap rocks (Fig. 13B). A good positive correlation between porosity and permeability characterizes the simple wave-like stylolite-bearing cap rocks (Fig. 13D). Comparing these results with the porosity and permeability tests of carbonate cap rocks from a previous study (Wu et al., 2019), and the relations between stylolite type and porosity and permeability, we

can conclude that: (1) stylolite-bearing carbonate cap rocks exhibit lower porosity (0.57%) and permeability (0.026 mD) than stylolite-free carbonate cap rocks (3.32% and 0.968 mD), indicating that stylolites induce heterogeneity, resulting in a more complex pore structure network and interconnectivity; (2) stylolite-bearing carbonate cap rocks have strong heterogeneity and present significant anisotropy, which are significantly different from those of stylolite-free cap rocks (Wu et al., 2018a); (3) permeability anisotropy is not only visible in rock units or reservoirs (Heap et al., 2018), but also arises between various types of stylolites in the same carbonate cap rock unit. Hence, the occurence of stylolites is an effective indicator for the heterogeneity of carbonate cap rocks.

5.3 Impact of stylolite types on the rock's pore structure

Significant differences of cumulative permeability contribution exist between the four types of stylolite samples. The influence of different types of stylolites on permeability can be reflected in the distribution of the dominant pores. Specifically, (1) transitional pore-II structures serve as the dominant pore type for rectangular layer type stylolites ; (2) macropores-I are the main pore type in seismogram pinning type stylolites; (3) mesopores-I and mesopores-II dominate in for suture & sharp peak type stylolites; and (4) transitional pore-II and micropores are the dominant pore type for simple wave-like type stylolites.

The average pore radius and threshold pressure are two important parameters for

the evaluation of the pore structure of rocks. In terms of average pore radius, rock samples containing the four types of stylolites can be ranked as follows: seismogram pinning type > suture & sharp peak type > rectangular layer type > simple wave-like type (Fig. 11). In terms of threshold pressure, rock samples containing the four types of stylolites can be arranged as follows: simple wave-like type > rectangular layer type > suture & sharp peak type > seismogram pinning type. The order of threshold pressure is perfectly consistent with that of the cover coefficient (Table 3), implying that the sealing capacity of carbonate cap rocks is strongly controlled by their pore structure. The pore size distribution and cumulative permeability contribution determine the sealing effectiveness of rocks capping carbonate reservoirs. Carbonate cap rocks bearing simple wave-like type stylolites have a better sealing capacity than those with seismogram pinning type stylolites because the former ones have a considerably narrow pore size distribution (0.0063-0.025 μm) and the latter ones show multiple peaks in a wide range (0.0063-63 μm). As mentioned above, the threshold pressure of cap rocks is controlled by their pore structures, and the pore structure has a close relationship with lithology type. Meanwhile, the lithology types are affected by lithogic fabric, which plays a key role in the formation of stylolite morphology.

5.4 Sealing effectiveness of cap rocks in relation to stylolite type

5.4.1 Controlling factors of sealing effectiveness

(1) Calcite and siliceous cementation

Previous studies of the diagenetic alterations of carbonate cap rocks in the Tarim Basin revealed that calcite cements can be found as fibrous to bladed, isopachous, blocky and drusy cements (Wu et al., 2018b). As typical diagenetic products formed under marine phreatic conditions, isopachous calcite cements established a strong framework against mechanical compaction, as proven by Beigi et al. (2017). Blocky calcite cements are mainly composed of medium to coarse crystals that fill intergranular pores and microfractures locally. Drusy cements, formed in the early diagenetic stage and also during burial, significantly contribute to the porosity reduction by completely or partially filling vuggy and intergranular pores. Abundant cementation is a major factor in lithologic densification of carbonate cap rocks. Calcite crystals easily soluble in acidic geological fluids were transported out with carbonate fluids (Wang et al., 2017). During chemical compaction, stylolites not only provide flow paths for the long-distance migration of dissolved materials, but also provide material for the subsequent burial cementation (Fabricius and Borre, 2007; Vandeginste and John, 2013). The dissolved materials precipitate into the pore space of the adjacent rock when burial temperature and pressure change (Mallon and Swarbrick, 2008), thereby making the stylolite-bearing cap rock intervals tight,

relative to the original host rock.

In addition, veins are completely filled with calcite cements and can act as barriers for fluid flow. This is demonstrated by the fact that the siliceous fluid migrated upwards along fractures but terminated at stylolites (Fig. 7I). Suture & sharp peak stylolites occlude migration channels, and siliceous mass is developed because of upward migration of siliceous fluid along the fractures. Therefore, tight zones in relation to stylolites show occlusion potential to fluid migration. This behavior is also shown for stylolites in the Smackover Formation where tight cement zones surrounding stylolites reduce the permeability by more than three orders of magnitude (Corwin et al., 1997).

(2) Occlusion of insoluble/sealing materials

The stylolite-dominated carbonate cap rocks became tight because of the combination of the progressively increasing overburden pressure from overlying sediments and pervasive cementation. Han et al. (2019) documented that calcite precipitated in dissolution pores and fractures has heavy $\delta^{18}O_{PDB}$ isotopic signature and low $^{87}Sr/^{86}Sr$, indicating an influence of formation water. Formation water mixed with with CO_2 and H_2S, together with organic fluids during organic matter maturation become acidic (Chen et al., 2003). Ruan et al. (2013) reported the pH of formation water in this study range from 5.0 to 6.5. The presence of acidic fluids resulted in dissolution of calcite during chemical compaction, and its transport along the pressure-solution surface. The occurrence of dolomite crystals replacing the calcite

matrix resulted from the entry of less saturated Mg/Ca fluids (Sibley and Gregg, 1987). Wu et al. (2018b) proposed a conceptual model for the characterization of the relationship between dolostones and stylolites that can be divided into four stages. Stage (1): rhombic dolomite crystals are scattered in the host limestone due to partial dolomitization. The formation of dolomite crystals is independent from the chemical compaction process. Stage (2): numerous rhombic dolomite crystals have less solubility than calcite and they are more likely to be concentrated in the vicinity of stylolites. Stage (3): Stylolites provide channels for hydrocarbon migration and organic acid fluids, which lead to some of the rhombic dolomite crystals being coated by pyrobitumen, while other crystals are partially corroded and without obvious rhombic shape. As chemical compaction proceeded, insoluble constituents accumulated along the solution surfaces. Gao et al. (2014) confirmed that the carbonate matrix of the study rocks has a low content of 0.2%-14.18% (with avg. 6.04%) of insoluble material by digesting samples in acid. Insolubles within stylolites present a variation from 2.10% to 76.54% (with avg. 34.00%). The more insoluble clay and pyrite crystals are enriched within stylolites relative to the matrix, while the content of calcite within stylolites is less than that of the matrix. Enrichment of dolomite, pyrite and organic matter along stylolites gradually reduced the permeability for flow across the stylolites (cf. Alsharhan and Sadd, 2000; Ebner et al., 2010; Heap et al., 2014). Stage (4): residual pores are completely filled with calcite cements, and stylolites act as barriers in the vertical direction. Intense stylolitization

thus results in a loss of porosity, the reduction of permeability and overall reduction of bed thickness or rock volume. Hence, the stylolite-controlled intervals exhibit permeability anisotropy (Gao et al., 2014) and behave as barriers that prevent fluid movements in both vertical and horizontal directions (Bruna et al., 2019).

(3) Dissolution and microfractures

The existence of diagenetic products along stylolites indicates that stylolitization and the calcite and dolomite cement filling the microfactures are related to fluid flow (Paganoni et al., 2016). The intensity of dissolution mainly depends on the reactive conditions and on the time when the long-term fluid-rock interaction reaches dynamic equilibrium (Credoz et al., 2009). A closed system is disadvantageous for the interaction between fluid and rocks. Although the dissolution of carbonate minerals can provide cement in the cap rocks, dissolution also results in the effective connection of pore space. Pervasive microfractures connected with isolated moldic and vuggy porosity will generally locally form higher porosity zones compared with the tight host rocks. Heap et al. (2014) reported that fracture networks around stylolites increase the permeability along the stylolitic plane, resulting in the formation of effective pathways for fluid flow and hydrocarbon migration. Some partially open veins with remaining porosity are connected with microfractures, which contribute to enhance permeability. This result is also in agreement with the conclusion of van der Voet et al. (2020).

5.4.2 Relationship between stylolite type and cover coefficient

(1) Rectangular layer type

Rectangular layer type stylolites show a variability in their sealing performance and can be divided into three segments: good sealing, moderate sealing and poor sealing (Fig. 14A, Table 4). Good sealing is found along stylolite teeth tips, where layer remnants are pervasively distributed. Sealing (insoluble) materials are collected at the bottom and top of stylolite teeth and stylolites act as effective fluid flow barriers as they enhance the sealing capacity of pinning layers. This was previously been proposed by Koehn et al. (2016) and Humphrey et al. (2019) for mudstones of the Permian Zechstein Basin (Germany). Moderate sealing is found in segments where some calcite veins are distributed parallel to the flanks of stylolites and a large amount of dark material (pyrobitumen and pyrite) is present at their teeth. Poor sealing segments always display that neither calcite cements nor pyrobitumen are visible at the teeth flanks. The offset layers in rectangular layer stylolites can create new fluid pathways together with partially-filled microfractures, which cause local leaking and destroy the sealing potential. Consequently, this rectangular layer type stylolite tends to cause heterogeneity of permeability.

(2) Seismogram pinning type

Seismogram pinning type stylolites present a complex sealing behavior and can be divided in two segments with moderate sealing and poor sealing, respectively (Table 4). In the moderately sealing segment, precipitation of sealing materials occurs

at the pronounced high-amplitude stylolite teeth and medium surface, which implies that the fluids flow across the stylolite is inhibited. Koehn et al. (2016) revealed that the amount and nature of material concentrated in stylolites determine the structuring of the median surface. In the poorly sealing segment, only median surfaces may form local efficient barriers for fluid flow if they can collect a large amount of insoluble material. These insoluble materials range from 0.1 to 1.3 cm in size and show patchy distributions in 2D through the observation of cross-sections of drill cores. This can be explained by: (i) as dilatant sites, it is generally believed that stylolite flanks are potential fluid pathways. The stylolite flanks have a poor sealing potential owing to their offset and lack of insoluble residues along them (Fig. 14B); (ii) dissolution holes triggered by leaching and burial fluids are located at the stylolite flanks. Partially-filled veins indicate that the fluid from which calcite precipitated once traveled along the steep teeth and precipitated at the flanks of stylolite teeth. This type of stylolite typically shows a highly variable local permeability.

(3) Suture & sharp peak type

Suture & sharp peak type stylolites can be divided in two segments, with good sealing and moderate sealing properties (Table 4). The sealing capacity probably depends on the volume of insoluble material that is collected by the stylolite and by what the properties of these materials are. When abundant sealing materials (e.g., insoluble clay-rich residuals) and surrounding precipitation of cements are collected and accumulated, stylolites appear as efficient fluid-flow barriers and have a good

sealing behavior (Fig. 14C). This observation is supported by flow simulations of very thin cement zones around the stylolite controlling large-scale flow and potential oil recovery (Corwin et al., 1997). Local precipitation of cements alone the pressure-solution interfaces only contributes to the limited reduction of porosity and permeability, thus providing an obstacle for regional fluid flow. Therefore, fluid or hydrocarbon leaks occur in the segments of sharp peaks where not enough impermeable materials are present and/or sealing materials are offset by spikes.

(4) Simple wave-like type

Park and Schot (1968) reported that the thickness of residues negatively correlate with stylolite amplitude. This can be explained by the fact that simple wave-like stylolites with extremely low amplitudes can have thicker residues than the other three types of stylolites. Extremely low-amplitude stylolites are arranged in parallel, often along bedding planes. Furthermore, the stylolite density increases with burial depth and such stylolites tend to show higher connectivity than the other types, forming anastomosing networks (Humphrey et al., 2020; Gomez-Rivas et al., 2022). Alsharhan and Sadd (2000) confirmed that carbonate rocks with high stylolite density are more likely to present lower permeability. Permeability across simple wave-like stylolites is more homogeneous than the first three types, with a higher coefficient of determination as shown in Fig. 13D. The stylolites formed at deep burial cut previously formed stylolites and terminate at or merge into clay particles. Thus, these stylolites can form at multiple stages and most of them are mainly filled with

869 insoluble pyrobitumen residue. Hence, simple wave-like type stylolites become very continuous and effective barriers for fluid flow (Fig. 14D) (*e.g.*, Humphrey et al., 2020; Gomez-Rivas et al., 2022).

6 Conclusions

(1) Four lithologies of stylolite-bearing carbonate cap rocks have been identified, with wackestone to packstone being the ones with most abundant stylolites, followed by mudstone, grainstone, and dolomitic limestone. Four stylolite types are identified: the simple wave-like type is the most common, followed by the seismogram pinning, suture & sharp peak and rectangular layer types in order of abundance. The formation of stylolites is significantly dependent on their host rock lithology. The rectangular layer type and seismogram pinning type stylolites are abundant in peloidal and intraclastic grainstone, while the suture & sharp peak type and simple wave-like type stylolites dominate in wackestone to packstone, respectively. The pore structure of stylolite-bearing carbonate cap rocks have multiscale variability in terms of pore size and connectivity. The four stylolite types correspond to four pore structure types based on the morphology of high-pressure mercury intrusion porosimetry curves. Samples bearing rectangular layer type stylolites are dominated by transitional pores-II, samples bearing simple wave-like type stylolites are dominated by transitional pores-II and micropores. Samples bearing seismogram pinning type stylolites are dominated by macropores-I. Samples bearing suture & sharp peak type

stylolites are dominated by mesopores-I and mesopores-II.

(2) Three factors affect the sealing effectiveness of carbonate cap rocks: (i) calcite and siliceous cements that precipitate in the pore space in the vicinity of stylolites, forming tight zones in relation to stylolites that show occlusion potential to fluid migration; (ii) insoluble/sealing material that accumulates along the pressure-solution seams and thus reduce the permeability for flow across the stylolites; and (iii) the connection of dissolution pores and microfractures along stylolites that provide effective pathways for fluid flow and hydrocarbon migration.

(3) In terms of sealing effectiveness the influence of the four stylolite types can be ranked as follows: simple wave-like type > rectangular layer type > suture & sharp peak type > seismogram pining type. However, the influence of stylolite segments on the rock sealing properties may differ from one segment to another. Rectangular layer type stylolites are divided into three segments (good, moderate and poor sealing). Both seismogram pining and suture & sharp peak stylolite types can be divided in two segments, with the former corresponding to moderate to poor sealing and the latter one to good and moderate sealing. Simple wave-like type stylolites present good sealing properties. The segments with good sealing potential correspond to the places where there are abundant insoluble residues and also where cements precipitated in the vicinity of stylolites. The segments with moderate sealing potential correspond to the places where insoluble residues and local cements are offset by spikes. The segments with poor sealing potential correspond to the places where the offset layers

create new fluid pathways together with partially-filled microfractures, which cause local leaking and destroy the sealing potential. This highlights that to determine the sealing potential of stylolites it is imperative to consider their geometry in detail.

Acknowledgements

This study was supported by the National Natural Science Foundation of China (42102151, 41802155, 41972130 and U19B6003), DGICYT Spanish Projects PGC2018-093903-B-C22 and PID2020-118999GB-I00 (Ministerio de Ciencia e Innovación, Agencia Estatal de Investigación, Fondo Europeo de Desarrollo Regional, Unión Europea) and the Grup Consolidat de Recerca "Geologia Sedimentària" (2017-SGR-824). Jun Wu also appreciate the China Scholarship Council (201806400037) for providing financial support during his study at the University of Barcelona. EGR acknowledges funding by the Spanish Ministry of Science, Innovation and Universities ("Ramón y Cajal" fellowship RYC2018-026335-I). We would like to thank GSA Bulletin Science Editor Wenjiao Xiao, Associate Editor and two anonymous reviewers, whose constructive suggestions and critical comments that significantly improved the paper.

References

Aguilera, R., 2006, Sandstone vs. carbonate petroleum reservoirs: A global perspective on porosity-depth and porosity-permeability relationships: Discussion*: AAPG Bulletin, v. 90, p. 807–810, https://doi.org/10.1306/09140505131.

Ahmatjan, A., Zhong, J.H., Li, Y., and Chen, X., 2010, Stylolite characteristics and petroleum geology significance of Ordovician carbonate rocks in Tahe Oilfield: Journal of China University of Petroleum (Edition of Natural Science), v. 34, no. 1, p. 7-11.

Alsharhan, A.S., Sadd, J.L., 2000, Stylolites in Lower Cretaceous carbonate reservoir, U.A.E., in proceeding: Middle East Models of Jurassic/Cretaceous Carbonate System. SEPM (Society for Sedimentary Geology), p. 185–207.

Beigi, M., Jafarian, A., Javanbakht, M., Wanas, H.A., Mattern, F., and Tabatabaei, A., 2017, Facies analysis, diagenesis and sequence stratigraphy of the carbonate-evaporite succession of the Upper Jurassic Surmeh Formation: Impacts on reservoir quality (Salman Oil Field, Persian Gulf, Iran): Journal of African Earth Sciences, v. 129, p. 179–194, https://doi.org/10.1016/j.jafrearsci.2017.01.005.

Beaudoin, N., Gasparrini, M., David, M.-E., Lacombe, O., and Koehn, D., 2019, Bedding-parallel stylolites as a tool to unravel maximum burial depth in sedimentary basins: Application to Middle Jurassic carbonate reservoirs in the Paris basin, France: GSA Bulletin, v. 131, p. 1239–1254, https://doi.org/10.1130/B32064.1.

Bihanni A., and Daigle H., 2019, On the role of spatially correlated heterogeneity in determining mudrock sealing capacity for CO_2 sequestration: Marine and Petroleum Geology, v. 106, p. 116–127, https://doi.org/10.1016/j.marpetgeo.2019.04.038.

Bruna, P.-O., Guglielmi, Y., Lamarche, J., Floquet, M., Fournier, F., Sizun, J.-P., Gallois, A., Marié, L., Bertrand, C., and Hollender, F., 2013, Porosity gain and loss in unconventional reservoirs: Example of rock typing in Lower Cretaceous hemipelagic limestones, SE France (Provence): Marine and Petroleum Geology, v. 48, p. 186–205, https://doi.org/10.1016/j.marpetgeo.2013.08.008.

Bruna, P.-O., Lavenu, A.P.C., Matonti, C., and Bertotti, G., 2019, Are stylolites fluid-flow efficient features? Journal of Structural Geology, v. 125, p. 270–277, https://doi.org/10.1016/j.jsg.2018.05.018.

Cao, Y., Wang, S., Zhang, Y., Yang, M., Yan, L., Zhao, Y., Zhang, J., Wang, X., Zhou, X., and Wang, H., 2019, Petroleum geological conditions and exploration potential of Lower Paleozoic carbonate rocks in Gucheng Area, Tarim Basin, China: Petroleum Exploration and Development, v. 46, p. 1165–1181, https://doi.org/10.1016/S1876-3804(19)60271-5.

Cazarin, C.L., Bezerra, F.H.R., Borghi, L., Santos, R.V., Favoreto, J., Brod, J.A., Auler, A.S., and Srivastava, N.K., 2019, The conduit-seal system of hypogene karst in Neoproterozoic carbonates in northeastern Brazil: Marine and Petroleum Geology, v. 101, p. 90–107, https://doi.org/10.1016/j.marpetgeo.2018.11.046.

Chen, Q., Qian, Y., Ma, H., and Wang, S., 2003, Diagenesis and porosity evolution of the Ordovician carbonate rocks in Tahe Oilfield, Tarim Basin: Petroleum Geology & Experiment, v. 25, no. 6, p. 729-734.

Cheng, Q.Q., Chen, H.Y., Fan M., Wang, Q., and Chen, W.J., 2006, Determination of the total pore texture of caprock: Petroleum Geology & Experiment, v. 28, no. 6, p. 604-608.

Corwin, L.W., Broomhall, R.W., Saidikowski, R.M., Wooten, J.N., 1997, Stylolites Impact the Miscible Nitrogen Flood in a Mature Carbonate Oil Field: Proceedings of the Middle East Oil

Show.

Credoz, A., Bildstein, O., Jullien, M., Raynal, J., Pétronin, J.C., Lillo, M., Pozo, C., and Geniaut, G., 2009, Experimental and modeling study of geochemical reactivity between clayey caprocks and CO_2 in geological storage conditions: Energy Procedia, v. 1, p. 3445–3452, https://doi.org/10.1016/j.egypro.2009.02.135.

Dong, S., Chen, D., Qing, H., Zhou, X., Wang, D., Guo, Z., Jiang, M., and Qian, Y., 2013, Hydrothermal alteration of dolostones in the Lower Ordovician, Tarim Basin, NW China: Multiple constraints from petrology, isotope geochemistry and fluid inclusion microthermometry: Marine and Petroleum Geology, v. 46, p. 270–286, https://doi.org/10.1016/j.marpetgeo.2013.06.013.

Du, Y., Fan, T., and Gao, Z., 2016, Geochemical characteristics and their implications to diagenetic environment of Lower-Middle Ordovician carbonate rocks, Tarim Basin, China: A case study of Bachu Dabantage outcrop and Aksu Penglaiba outcrop: Natural Gas Geoscience, v. 27, no. 8, p. 1509–1523.

Ebner, M., Piazolo, S., Renard, F., and Koehn, D., 2010, Stylolite interfaces and surrounding matrix material: Nature and role of heterogeneities in roughness and microstructural development: Journal of Structural Geology, v. 32, p. 1070–1084, https://doi.org/10.1016/j.jsg.2010.06.014.

Ehrenberg, S.N., Morad, S., Yaxin, L., and Chen, R., 2016, Stylolites and porosity in a Lower Cretaceous Limestone Reservoir, Onshore Abu Dhabi, U.A.E.: Journal of Sedimentary Research, v. 86, p. 1228–1247, https://doi.org/10.2110/jsr.2016.68.

Ehrenberg, S.N., and Wu, Q., 2019, Dense zones of the Kharaib Formation (Lower Cretaceous), United Arab Emirates: Journal of Sedimentary Research, v. 89, p. 353–380, https://doi.org/10.2110/jsr.2019.20.

Ellis, B.R., Fitts, J.P., Bromhal, G.S., McIntyre, D.L., Tappero, R., and Peters, C.A., 2013, Dissolution-driven permeability reduction of a fractured carbonate caprock: Environmental Engineering Science, v. 30, no. 4, p. 187-193, https://doi.org/10.1089/ees.2012.0337.

Fabricius, I.L., and Borre, M.K., 2007, Stylolites, porosity, depositional texture, and silicates in chalk facies sediments. Ontong Java Plateau—Gorm and Tyra fields, North Sea: Sedimentology, v. 54, p. 183-205, https://doi.org/10.1111/j.1365-3091.2006.00828.x.

Fan, Z.Y., Lin, C.Y., Ju, C.X., Han, C.C., and Xiong, C.W., 2017, Characteristic of main Ordovician reservoir rocks in Block Two of Tahe oilfield: Journal of Jilin University (Earth Science Edition), v. 47, no. 1, p. 37-47.

Gao, G., Liu, G.D., Wang, C.Y., and Shi, S.B., 2014, A comparative study of the organic matter characteristics of stylolite and matrix in carbonate rock: Nature Gas Geoscience, v. 25, no. 8, p. 1205-1209.

GB/T 29171-2012, 2012. Rock capillary pressure measurement. China Standard Press, Beijing.

GB/T 27172-2012, 2013. Practices for core analysis. China Standard Press, Beijing.

Gomez-Rivas, E., Martín-Martín, J.D., Bons, P.D., and Koehn, D. 2015, Can stylolite networks control the geometry of hydrothermal alterations? Geotectonic Research, v. 97, no. 1, p. 34-36. https://doi.org/10.1127/1864-5658/2015-13.

Gomez-Rivas, E., Martín-Martín, J.D., Bons, P.D., Koehn, D., Griera, A., Travé, A., Llorens, M.-G., Humphrey, E., and Neilson, J., 2022, Stylolites and stylolite networks as primary controls on the geometry and distribution of carbonate diagenetic alterations: Marine and Petroleum Geology, v. 136, p. 105444, https://doi.org/10.1016/j.marpetgeo.2021.105444.

Grunau, H.R., 1987, A Worldwide Look at the Cap-rock Problem: Journal of Petroleum Geology, v. 10, no. 3, p. 245-265, https://doi.org/10.1111/j.1747-5457.1987.tb00945.x.

Han, C., Lin, C., Lu, X., Tian, J., Ren, L., and Ma, C., 2019, Petrological and geochemical constraints on fluid types and formation mechanisms of the Ordovician carbonate reservoirs in Tahe Oilfield, Tarim Basin, NW China: Journal of Petroleum Science and Engineering, v. 178, p. 106–120, https://doi.org/10.1016/j.petrol.2019.03.010.

Han, Y., Li, Z., Liu, J., and Peng, S., 2013, Genesis of dolomites in limestone of Yingshan Formation and their effects on poroperm characteristics of carbonatereservoir in Tahe area: Chinese Journal of Geology, v. 48, no. 3, p. 721-731.

He, Z.L., Jin, X.H., Wo, Y.J., Li, H.L., Bai, Z.R., Jiao, C.L., and Zhang, Z.P., 2016, Hydrocarbon accumulation characteristics and exploration domains of ultra-deep marine carbonates in China: China Petroleum Exploration, v. 21, no. 1, p. 3-14.

Heap, M.J., Baud, P., Reuschlé, T., and Meredith, P.G., 2014, Stylolites in limestones: Barriers to fluid flow? Geology, v. 42, no. 1, p. 51–54, https://doi.org/10.1130/G34900.1.

Heap, M., Reuschlé, T., Baud, P., Renard, F., and Iezzi, G., 2018, The permeability of stylolite-bearing limestone: Journal of Structural Geology, v. 116, p. 81–93, https://doi.org/10.1016/j.jsg.2018.08.007.

Hollis, C., Vahrenkamp, V., Tull, S., Mookerjee, A., Taberner, C., and Huang, Y., 2010, Pore system characterisation in heterogeneous carbonates: An alternative approach to widely-used rock-typing methodologies: Marine and Petroleum Geology, v. 27, p. 772–793, https://doi.org/10.1016/j.marpetgeo.2009.12.002.

Humphrey, E., Gomez-Rivas, E., Koehn, D., Bons, P.D., Neilson, J., Martín-Martín, J.D., and Schoenherr, J., 2019, Stylolite-controlled diagenesis of a mudstone carbonate reservoir: A case study from the Zechstein_2_Carbonate (Central European Basin, NW Germany): Marine and Petroleum Geology, v. 109, p. 88–107, https://doi.org/10.1016/j.marpetgeo.2019.05.040.

Humphrey, E., Gomez-Rivas, E., Neilson, J., Martín-Martín, J.D., Healy, D., Yao, S., and Bons, P.D., 2020, Quantitative analysis of stylolite networks in different platform carbonate facies: Marine and Petroleum Geology, v. 114, p. 104203, https://doi.org/10.1016/j.marpetgeo.2019.104203.

Janjuhah, H.T., Alansari, A., Ghosh, D.P., and Bashir, Y., 2018, New approach towards the classification of microporosity in Miocene carbonate rocks, Central Luconia, offshore Sarawak, Malaysia: Journal of Natural Gas Geoscience, v. 3, p. 119–133, https://doi.org/10.1016/j.jnggs.2018.05.001.

Jiao, F.Z., 2018, Significance and prospect of ultra-deep carbonate fault-karst reservoirs in Shunbei area, Tarim Basin: Oil & Gas Geology, v. 39, no. 2, p. 207-2016.

Klokov, A., Treviño, R.H., and Meckel, T.A., 2017, Diffraction imaging for seal evaluation using

ultra high resolution 3D seismic data: Marine and Petroleum Geology, v. 82, p. 85–96, https://doi.org/10.1016/j.marpetgeo.2017.02.002.

Koehn, D., Rood, M.P., Beaudoin, N., Chung, P., Bons, P.D., and Gomez-Rivas, E., 2016, A new stylolite classification scheme to estimate compaction and local permeability variations: Sedimentary Geology, v. 346, p. 60–71, https://doi.org/10.1016/j.sedgeo.2016.10.007.

Lan, X.D., and Lü, X.X., 2014, Carbonate sealing and its controlling factors: cap rock and inner barrier layers of Yingshan Formation on Tazhong Northern Slope, Tarim Basin: Turkish Journal of Earth Sciences, v. 23, no. 6, p. 581-601, https://doi.org/10.3906/yer-1312-12.

Laronne Ben-Itzhak, L., Aharonov, E., Toussaint, R., and Sagy, A., 2012, Upper bound on stylolite roughness as indicator for amount of dissolution: Earth and Planetary Science Letters, v. 337–338, p. 186–196, https://doi.org/10.1016/j.epsl.2012.05.026.

Laronne Ben-Itzhak, L., Aharonov, E., Karcz, Z., Kaduri, M., and Toussaint, R., 2014, Sedimentary stylolite networks and connectivity in limestone: Large-scale field observations and implications for structure evolution: Journal of Structural Geology, v. 63, p. 106–123, https://doi.org/10.1016/j.jsg.2014.02.010.

Leythaeuser, D., Borromeo, O., Mosca, F., di Primio, R., Radke, M., and Schaefer, R.G., 1995, Pressure solution in carbonate source rocks and its control on petroleum generation and migration: Marine and Petroleum Geology, v. 12, p. 717–733, https://doi.org/10.1016/0264-8172(95)93597-W.

Li, C.H., Zhao, L., Li, W.Q., Li, J.X., Ding, Y.T., Li, A., and Qi, Y.P., 2019, Research status and its significance to oilfield development of stylolite in carbonate: Natural Gas Geoscience, v. 30, no. 4, p. 493-502.

Li, Y., Xue, Z.J., Cheng, Z., Jiang, H.J., and Wang, R.Y., 2020, Progress and development directions of deep oil and gas exploration and development in China: China Petroleum Exploration, v. 25, no. 1, p. 45-57.

Liu, S.J., Gao, G., Gang, W.Z., Qu, T., Dang, W.L., Zhang, W.W., Yang, S.R., and Zhu, K.L., 2020a, Implications of organic matter source and fluid migration from geochemical characteristics of stylolites and matrix in carbonate rocks: A case study from the Carboniferous and the Ordovician in the Sichuan Basin, SW China: Journal of Petroleum Science and Engineering, v. 186, p. 106606, https://doi.org/10.1016/j.petrol.2019.106606.

Liu, X.L., and Lü, X.B., 2010, Volume calculation method for fracture-cavity reservoir body in Tahe Oilfield, Tarim Basin: Xinjiang Petroleum Geology, v. 31, p. 593-595.

Liu, Y.L., You, D.H., Gao, L.J., Zhang, W.F., and Xie, C.F., 2020b, Genesis and geological significance of siliceous rock in Penglaiba Formation in Well Tashen 6, Tahe oilfield: Oil & Gas Geology, v. 41, no. 1, p. 83-91.

Lü, H.T., Ding, Y., and Geng, F., 2014, Hydrocarbon accumulation patterns and favorable exploration areas of the Ordovician in Tarim Basin: Oil & Gas Geology, v. 35, no. 6, p. 798-805.

Lü, X.X., Wang, Y.F., Yu, H.F., and Bai, Z.K., 2017, Major factors affecting the closure of marine carbonate caprock and their quantitative evaluation: A case study of Ordovician rocks on the northern slope of the Tazhong uplift in the Tarim Basin, western China: Marine and

Petroleum Geology, v. 83, p. 231–245, https://doi.org/10.1016/j.marpetgeo.2017.03.006.

Lü, X.X., Chen, P.P., Chen, K., Zhang, J., and Qian, W.W., 2019, Effects of differential diagenesis of deep carbonate rocks on hydrocarbon zonation and accumulation: A case study of Yingshan Formation on northern slope of Tazhong uplift, Tarim Basin: Oil & Gas Geology, v. 40, no. 5, p. 957-971.

Makhloufi, Y., Collin, P.-Y., Bergerat, F., Casteleyn, L., Claes, S., David, C., Menendez, B., Monna, F., Robion, P., Sizun, J.-P., Swennen, R., and Rigollet, C., 2013, Impact of sedimentology and diagenesis on the petrophysical properties of a tight oolitic carbonate reservoir. The case of the Oolithe Blanche Formation (Bathonian, Paris Basin, France): Marine and Petroleum Geology, v. 48, p. 323–340, https://doi.org/10.1016/j.marpetgeo.2013.08.021.

Mallon, A.J., and Swarbrick, R.E., 2008, Diagenetic characteristics of low permeability, non-reservoir chalks from the Central North Sea: Marine and Petroleum Geology, v. 25, p. 1097–1108, https://doi.org/10.1016/j.marpetgeo.2007.12.001.

Marfil, R., Caja, M.A., Tsige, M., Al-Aasm, I.S., Martín-Crespo, T., and Salas, R., 2005, Carbonate-cemented stylolites and fractures in the Upper Jurassic limestones of the Eastern Iberian Range, Spain: A record of palaeofluids composition and thermal history: Sedimentary Geology, v. 178, p. 237–257, https://doi.org/10.1016/j.sedgeo.2005.05.010.

Martín-Martín, J.D., Gomez-Rivas, E., Gómez-Gras, D., Travé, A., Ameneiro, R., Koehn, D., and Bons, P.D., 2018, Activation of stylolites as conduits for overpressured fluid flow in dolomitized platform carbonates: Geological Society Special Publication, v. 459, p. 157–176, https://doi.org/10.1144/SP459.3.

Matyszkiewicz, J., and Kochman, A., 2016, Pressure dissolution features in oxfordian microbial-sponge buildups with pseudonodular texture, kraków upland, Poland. Annales Societatis Geologorum Poloniae, v. 86, p. 355-377.

Mehrabi, H., Mansouri, M., Rahimpour-Bonab, H., Tavakoli, V., and Hassanzadeh, M., 2016, Chemical compaction features as potential barriers in the Permian-Triassic reservoirs of Southern Iran: Journal of Petroleum Science and Engineering, v. 145, p. 95–113, https://doi.org/10.1016/j.petrol.2016.03.020.

Menke, H., Bijeljic, B., Andrew, M., and Blunt, M.J., 2014, Dynamic pore-scale imaging of reactive transport in heterogeneous carbonates at reservoir conditions: Energy Procedia, v. 63, p. 5503-5511, http://dx.doi.org/10.1016/j.egypro.2014.11.583.

Morad, D., Nader, F.H., Morad, S., Al Darmaki, F., and Hellevang, H., 2018, Impact of Stylolitization On Fluid Flow and Diagenesis in Foreland Basins: Evidence from an Upper Jurassic Carbonate Gas Reservoir, Abu Dhabi, United Arab Emirates: Journal of Sedimentary Research, v. 88, p. 1345–1361, https://doi.org/10.2110/jsr.2018.70.

Morad, S., Al Suwaidi, M., Mansurbeg, H., Morad, D., Ceriani, A., Paganoni, M., and Al-Aasm, I., 2019. Diagenesis of a limestone reservoir (Lower Cretaceous), Abu Dhabi, United Arab Emirates: Comparison between the anticline crest and flanks: Sedimentary Geology, v. 380, p. 127–142, https://doi.org/10.1016/j.sedgeo.2018.12.004.

Nakayama, K., 1999, Evaluation of seal capacity for carbonate reservoir with salt seal in

Karachaganak Field, Kazakhstan: Energy Exploration & Exploitation, v. 17, no. 3-4, p. 283-300.

Ning, F., Yun, J.B., Li, J.J., and Song, H.M., 2018, New Method to Evaluate Carbonate Cap Rocks: Enlightenment from Rock Mechanical Property. In 2018 AAPG International Conference and Exhibition.

Niu, Y., Zhong, J., Wang, P., Shan, T., and Li, R., 2010, Effect of diagenesis on accumulate capability of Ordovician carbonate rock in Block 2 of Tahe Oilfield: Journal of China University of Petroleum, v. 34, no. 6, p. 13-19.

Paganoni, M., Al Harthi, A., Morad, D., Morad, S., Ceriani, A., Mansurbeg, H., Al Suwaidi, A., Al-Aasm, I.S., Ehrenberg, S.N., and Sirat, M., 2016, Impact of stylolitization on diagenesis of a Lower Cretaceous carbonate reservoir from a giant oilfield, Abu Dhabi, United Arab Emirates: Sedimentary Geology, v. 335, p. 70–92, https://doi.org/10.1016/j.sedgeo.2016.02.004.

Park, W.C., and Schot, E.H. 1968, Stylolites: their nature and origin: Journal of Sedimentary Research, v. 38, p. 175–191, https://doi.org/10.1306/74D71910-2B21-11D7-8648000102C1865D.

Peacock, D.C.P., and Azzam, I.N., 2006, Development and scaling relationships of a stylolite population: Journal of Structural Geology, v. 28, p. 1883–1889, https://doi.org/10.1016/j.jsg.2006.04.008.

Qi, L.X., 2016, Oil and gas breakthrough in ultra-deep Ordovician carbonate formations in Shuntuoguole uplift, Tarim: China Petroleum Exploration, v. 21, no. 3, p. 38-51.

Qian, Y.X., He, Z.L., Chen, Q.L., Li, H.L., Lu, Q.H., Cai, X.R., and You, D.H., 2012, Sealing capacity of the Ordovician carbonate rocks in Tazhong area, the Tarim Basin: Oil & Gas Geology, v. 33, no. 1, p. 1-9, and 18.

Rashid, F., Glover, P.W.J., Lorinczi, P., Collier, R., and Lawrence, J., 2015, Porosity and permeability of tight carbonate reservoir rocks in the north of Iraq: Journal of Petroleum Science and Engineering, v. 133, p. 147–161, https://doi.org/10.1016/j.petrol.2015.05.009.

Rashid, F., Glover, P.W.J., Lorinczi, P., Hussein, D., and Lawrence, J.A., 2017, Microstructural controls on reservoir quality in tight oil carbonate reservoir rocks: Journal of Petroleum Science and Engineering, v. 156, p. 814–826, https://doi.org/10.1016/j.petrol.2017.06.056.

Railsback, L.B., 1993, Lithologic controls on morphology of pressure-dissolution surfaces (stylolites and dissolution seams) in Paleozoic carbonate rocks from the mideastern United States: Journal of Sedimentary Research, v. 63, p. 513–522, https://doi.org/10.2110/jsr.63.513.

Ronchi, P., and Cruciani, F., 2015, Continental carbonates as a hydrocarbon reservoir, an analog case study from the travertine of Saturnia, Italy: AAPG Bulletin, v. 99, p. 711–734, https://doi.org/10.1306/10021414026.

Ruan, Z., Yu, B., Wang, L., Pan, Y., and Tan, G., 2013, Prediction of buried calcite dissolution in the Ordovician carbonate reservoir of the Tahe Oilfield, NW China: Evidence from formation water: Geochemistry, v. 73, p. 469–479, https://doi.org/10.1016/j.chemer.2013.03.004.

Rustichelli, A., Tondi, E., Korneva, I., Baud, P., Vinciguerra, S., Agosta, F., Reuschlé, T., and

Reuschlé, T., 2015, Bedding-parallel stylolites in shallow-water limestone successions of the Apulian Carbonate Platform (central-southern Italy): Italian Journal of Geosciences, v. 134, p. 513–534, https://doi.org/10.3301/IJG.2014.35.

Sassen, R., and Moore, C.H., 1988, Framework of hydrocarbon generation and destruction in eastern Smackover trend: AAPG Bulletin, v. 72, p. 649–663, https://doi.org/10.1306/703C8EF7-1707-11D7-8645000102C1865D.

Schlömer, S., and Krooss, B.M., 1997, Experimental characterisation of the hydrocarbon sealing efficiency of cap rocks: Marine and Petroleum Geology, v. 14, p. 565-580, https://doi.org/10.1016/S0264-8172(97)00022-6.

Shang, P., 2019, The coupling relationship between evolution of diagenetic fluid and hydrocarbon accumulation of Ordovician in Tahe Area, northern of Tarim Basin [Ph.D. thesis]: China University of Geosciences (Wuhan), 141p, doi: 10.27492/d.cnki.gzdzu.2019.000012.

Sheppard, T.H., 2002, Stylolite development at sites of primary and diagenetic fabric contrast within the Sutton Stone (Lower Lias), Ogmore-by-Sea, Glamorgan, UK: Proceedings of the Geologists' Association, v. 113, p. 97–109, https://doi.org/10.1016/S0016-7878(02)80013-X.

Sibley, D.F., and Gregg, J.M., 1987, Classification of dolomite rock textures: Journal of Sedimentary Research, v. 57, p. 967–975, https://doi.org/10.1306/212F8CBA-2B24-11D7-8648000102C1865D.

Smith, J.V., 2000, Three-dimensional morphology and connectivity of stylolites hyperactivated during veining: Journal of Structural Geology, v. 22, p. 59–64, https://doi.org/10.1016/S0191-8141(99)00138-8.

Tan, Q.Y., Wang, R.H., Mou, C.L., Cheng, J.X., Wang, Z.H., and Fu, J.Y., 2011, New consideration on the genesis of suture: Earth Science Frontiers, v. 18, no. 3, p. 241-249.

Tang, L.J., Guo, T.L., Tian, H.Q., Jin, W.Z., Li, R.F., Wan, G.M., Dong, L., and Wang, P.W., 2008, Polycycle tectonic evolution, differential deformation and hydrocarbon reservation of central Guizhou and adjacent region: Acta Geologica Sinica, v. 82,p. 298-307

Tang, L., Zhang, X., Long, G., Xu, F., Wang, B., Han, H., Xu, L., Yang, M., Li, H., and Wang, G., 2013, Pool features and hydrocarbon accumulation analysis of lacustrine carbonate rock: take Nanyishan reservior in Qaidam Basin as an example: Natural Gas Geoscience, v. 24, no. 3, p. 591-598.

Terzaghi, R.D., 1965. Sources of error in joint surveys: Geotechnique, v. 15, no. 3, p. 287-304, http://worldcat.org/issn/00168505.

Tian, F., Jin, Q., Lu, X.B., Lei, Y.H., Zhang, L.K., Zheng, S.Q., Zhang, H.F., Rong, Y.S., and Liu, N.G., 2016. Multi-layered ordovician paleokarst reservoir detection and spatial delineation: A case study in the Tahe Oilfield, Tarim Basin, Western China: Marine and Petroleum Geology, v. 69, p. 53–73, https://doi.org/10.1016/j.marpetgeo.2015.10.015.

Tonnet, N., Mouronval, G., Chiquet, P., and Broseta, D., 2011, Petrophysical assessment of a carbonate-rich caprock for CO_2 geological storage purposes: Energy Procedia, v. 4, p. 5422–5429, https://doi.org/10.1016/j.egypro.2011.02.527.

Toussaint, R., Aharonov, E., Koehn, D., Gratier, J.P., Ebner, M., Baud, P., Rolland, A., and Renard, F., 2018, Stylolites: A review: Journal of Structural Geology, v. 114, p. 163–195,

https://doi.org/10.1016/j.jsg.2018.05.003.

van der Voet, E., Muchez, P., Laenen, B., Weltje, G. J., Lagrou, D., and Swennen, R., 2020, Characterizing carbonate reservoir fracturing from borehole data–A case study of the Viséan in northern Belgium: Marine and Petroleum Geology, v. 111, p. 375–389, https://doi.org/10.1016/j.marpetgeo.2019.08.040.

Vandeginste, V., and John, C.M., 2013, Diagenetic Implications of Stylolitization in Pelagic Carbonates, Canterbury Basin, Offshore New Zealand: Journal of Sedimentary Research, v. 83, p. 226–240, https://doi.org/10.2110/jsr.2013.18.

Wang, M., and Yu, Q., 2017, Pore structure characterization of Carboniferous shales from the eastern Qaidam Basin, China: Combining helium expansion with low-pressure adsorption and mercury intrusion: Journal of Petroleum Science and Engineering, v. 152, p. 91–103, https://doi.org/10.1016/j.petrol.2017.02.007.

Wang, Q.L., Han, J.F., Li, H., Sun, Y.D., He, H.Q., and Ren, S.J., 2019, Carbonate sequence architecture, sedimentary evolution and sea level fluctuation of the Middle and Lower Ordovician on outcrops at the northwestern margin of Tarim Basin: Oil & Gas Geology, v. 40, no. 4, p. 835-850, 916.

Wang, Q.L., Lin, C.S., Li, H., Han, J.F., Sun, Y.D., and He, H.Q., 2018, Carbonate sedimentary microfacies characteristics and evolution of the Middle and Lower Ordovician in northwestern of Tarim Basin: Nature Gas Geoscience, v. 29, no. 9, p. 1274-1288.

Wang, X., Gao, G., Li, J.Y., Ge, D.W., and Zhang, W.W., 2017, Hydrocarbon explusion of stylolite and matrix in carbonate rocks: A case study from the Ordovician and Carboniferous carbonate rocks in Eastern Sichuan Basin: Oil & Gas Geology, v. 38, no. 3, p. 534-542.

Wilson, R.D., Chitale, J., Huffman, K., Montgomery, P., and Prochnow, S.J., 2020. Evaluating the depositional environment, lithofacies variation, and diagenetic processes of the Wolfcamp B and lower Spraberry intervals in the Midland Basin: Implications for reservoir quality and distribution: AAPG Bulletin, v. 104, p. 1287–1321, https://doi.org/10.1306/12031917358.

Wu, J., 2020, Carbonate cap rocks and controlling factors on sealing capacity: A case study of the Ordovician Yingshan Formation in northern Tarim Basin [Ph.D. thesis]: China University of Geosciences (Beijing), 180p, doi: 10.27493/d.cnki.gzdzy.2020.000047.

Wu, J., Fan, T.L., Gao, Z.Q., Gu, Y., Wang, J.B., Du, Y., Li, C., Wang, S.S., Zhang, C.J., Meng, M.M., Wei, D., and Fan, H., 2018a, Identification and characteristic analysis of carbonate cap rock: A case study from the Lower-Middle Ordovician Yingshan Formation in Tahe oilfield, Tarim Basin, China: Journal of Petroleum Science and Engineering, v. 164, p. 362–381, https://doi.org/10.1016/j.petrol.2017.12.070.

Wu, J., Fan, T.L., Gao, Z.Q., Yin, X.X., Fan, X., Li, C.C., Yu, W.Y., Li, C., Zhang, C.J., Zhang, J.H., and Sun, X.N., 2018b, A conceptual model to investigate the impact of diagenesis and residual bitumen on the characteristics of Ordovician carbonate cap rock from Tarim Basin, China: Journal of Petroleum Science and Engineering, v. 168, p. 226–245, https://doi.org/10.1016/j.petrol.2018.05.034.

Wu, J., Fan, T.L., Gomez-Rivas, E., Gao, Z.Q., Yao, S.Q., Li, W.H., Zhang, C.J., Sun, Q.Q., Gu, Y., and Xiang, M., 2019, Impact of pore structure and fractal characteristics on the sealing

capacity of Ordovician carbonate cap rock in the Tarim Basin, China: Marine and Petroleum Geology, v. 102, p. 557–579, https://doi.org/10.1016/j.marpetgeo.2019.01.014.

Wu, J., Fan, T.L., Gomez-Rivas, E., Travé, A., Gao, Z.Q., Wang, S.S., and Sun, X.L., 2021, Fractal characteristics of pore networks and sealing capacity of Ordovician carbonate cap rocks: a case study based on outcrop analogs from the Tarim Basin, China: AAPG Bulletin, v. 105, no. 2, p. 437–479, https://doi.org/10.1306/03172019022.

Yan, W., Wang, X.Z., Zhang, T.S., Ding, Y., Liu, C.G., and Lü, H.T., 2011, Investigations of the karst during the Episode III of the mid-Caledonian in the Tahe Oilfield: Acta Petrolei Sinica, v. 32, no. 3, p. 411-416.

Yang, C.Z., and Liu, X., 1991, A study of carbonate cap rocks of oil and gas: Natural Gas Industry, v. 11, no. 6, p. 17-23.

Ye, D., 1994, Deep dissolution of Cambrian-Ordovician carbonates in the northern Tarim Basin: Acta Sedimentologica Sinica, v. 12, no. 1, p. 66-71.

Zhang, X., Salemans, J., Peach, C. J., and Spiers, C. J., 2002, Compaction experiments on wet calcite powder at room temperature: evidence for operation of intergranular pressure solution: Geological Society, London, Special Publications, v. 200, no.1, p. 29-39, https://doi.org/10.1144/GSL.SP.2001.200.01.02.

Zhang, Z., Zhang, H., Li, J., and Cai, Z., 2021, Permeability and porosity prediction using logging data in a heterogeneous dolomite reservoir: An integrated approach: Journal of Natural Gas Science and Engineering, v. 86, p. 103743, https://doi.org/10.1016/j.jngse.2020.103743.

Zhou, X., Lü, X., Quan, H., Qian, W., Mu, X., Chen, K., Wang, Z., and Bai, Z., 2019, Influence factors and an evaluation method about breakthrough pressure of carbonate rocks: An experimental study on the ordovician of carbonate rock from the Kalpin area, Tarim Basin, China: Marine and Petroleum Geology, v. 104, p. 313-330, https://doi.org/10.1016/j.marpetgeo.2019.03.034.

Figure captions

Fig. 1 (A) Location map of the Tarim Basin, northwestrn China. The locations of outcrops in the northwestern margin of the Tarim Basin and the Tahe oilfield in the Tabei Uplift (Tarim Basin) are marked with dark blue and light blue shadows, respectively. (B) Large-scale location map of four outcrops (marked with four dark blue triangles), including the Penglaiba (PLB), Kepingshuinichang (KPSNC), Yangjikan (YJK) and Dabantage (DBTG) outcrops. (C) Large-scale location map of

the Tahe oilfield, in which the studied wells are marked with brown dots and cross section A-A' is marked with blue dotted line (modified from Wu et al., 2018a).

Fig. 2 (A) Detailed stratigraphy of the Lower-Upper Ordovician successions at the four outcrop sections in the Keping Uplift, Tarim Basin, including the lithology, sequence(Sq) stratigraphy and depositional evolution (modified from Wang et al., 2019; Wu et al., 2021); (B) Schematic diagram showing source rock, reservoir and cap rock assemblage from the Majiaer Depression to Tabei Uplift to Kuqa Depression in the Tarim Basin (the direction of Section A-A' is marked with blue dotted line in Fig. 1C, modified after Lü et al., 2014).

Fig. 3 (A) Schematic diagram of the burial history of the Tahe oilfield in the Tabei Uplift. The burial curve is shown in combination with homogenization temperatures of fluid inclusions, as well as the tectonic evolution of Ordovician rocks of the Tahe oilfield (modified from Chen et al., 2014; Wu et al., 2018b); (B) Burial history of the Ordovician Yingshan Formation and their four diagenetic stages at the Dabantage and Penglaiba outcrops in the Keping Uplift, northwestern margin of the Tarim Basin (modified after Ye et al., 1994; Dong et al., 2013; Du et al., 2016; Wu et al., 2021). Colored dotted lines in the bottom of the graphic represent a weaker degree of diagenesis than a stronger degree represented with solid lines.

Fig. 4 Stylolite type, number and stylolization-related diagenetic products between

carbonate cap rock intervals and reservoir intervals of the Lower-Middle Ordovician Yingshan Formation from the drill cores in the Tarim Basin.

Fig. 5 Thin-section photomicrograph of four carbonate cap rock lithologies containing stylolites (pink arrows) from the Ordovician Yingshan Formation. (A) Mudstone, homogeneous micrite, blocky cements filled the top of stylolite teeth and fenestrae pore; (B) Bioclastic wackestone, containing rectangular layer type and suture & sharp peak type stylolite as well as minor bioclast fragment; (C) Intraclastic packstone, showing bioclastic fragments and discontinuous simple wave-like type stylolite; (D) Seismogram pinning type stylolite acting as a lithologic boundary between peloidal grainstone and mudstone. Sample from well TS3 at 6115.56 m depth; (E) Intraclastic grainstone, these intraclasts were cut by suture & sharp peak type stylolites with high-amplitude; (F) Dolomitic limestone, dolomite-calcitised dolomite were embedded in pyrobitumen and euhedral dolomite crystals postdate the stylolite. Sample from well AD29 at burial depth of 6718.1 m; Samples (A), (B), (C) and (E) are from the Dabantage, Penglaiba, Kepingshuinichang, and Yanjikan outcrop, respectively.

Fig. 6 Stylolite characteristics of carbonate cap rocks from the Ordovician Yingshan Formation in the Tarim Basin. (A) Frequency abundances of stylolite morphology using the classification scheme by Koehn et al. (2016); (B) Frequency distribution of the stylolite density of carbonate cap rocks; (C) Frequency distribution of the stylolite amplitude of carbonate cap rocks; (D) Frequency distribution of the stylolite spacing of

carbonate cap rocks.

Fig. 7 Core photographs of four bedding-parallel stylolite types classified by Koehn et al. (2016) and diagenetic products in relation to stylolization within carbonate cap rocks of the Ordovician Yingshan Formation in the Tarim Basin. (A) Rectangular layer type. Stylolite acting as lithologic boundaries between peloidal grainstone and mudstone. High-amplitude stylolite containing straight flanks, and residual bitumen occurs within stylolite teeth. Sample from well AD11 at a depth of 6871.79 m; (B) Seismogram pinning type. Stylolites bound light grey calcitised dolomite and cut by calcite vein. Sample from well SN6 at 6850.55 m depth; (C) Suture & sharp peak type. Unconnected and interconnected stylolite networks occurs locally. Younger stylolite cannibalizes older one. Sample from well SN7 at a depth of 6871.79 m; (D) Simple wave-like type. Completely-filled microfracture cut by stylolite. Two stylolites (Sty. 1 and Sty. 2) are merged into one stylolite. Sample from well SN7 at 6547.59 m depth; (E) Calcite cements distributed below the crest of stylolites and infilling vugs. Sample from well SN6 at a burial depth of 6849.87-6850.07 m; (F) Bitumen embedded in the crest and trough of stylolites, and bitumen is absent in the flank of stylolites. Sample from well S88 at a depth of 6160.29-6160.42 m; (G) Clay is concentrated at the peak of stylolite. A swarm of completely-filled microfractures terminated at the stylolite. Sample from well S88 at a depth of 6154.93-6155.04 m; (H) Relationship of two calcite veins showing first vein cut by second one. Sample from well SN401 at a burial depth of

6631.76-6631.88 m; (I) Siliceous mass filling the fractures. Sample from well S88 at a burial depth of 6743.89-6744 m.

Fig. 8 Outcrop photographs and thin-section photomicrographs showing different morphology and density of stylolites and their related products associated with chemical compaction. (A) Bitumen accumulated in the peak of the stylolite, and calcite cements precipitated in dissolution vugs. Sample from the Yangjikan outcrop; (B) Dolomite crystals along a stylolite. Sample from the Dabantage outcrop; (C) Scattered dolomite crystals and open microfractures are clearly visible, and part of microfracture veins filled with calcite cements were cut by stylolites. Sample from the Penglaiba outcrop; (D) Euhedral to subhedral dolomite crystals are concentrated in the vicinity of stylolites. Sample from the Kepingshuinichang outcrop; (E) Pyrite crystals with size of 0.26 mm occurs within bitumen. Sample from the Kepingshuinichang outcrop; (F) Oxidized bitumen residue occurs within stylolites. Sample from the Dabantage outcrop.

Fig. 9 SEM photomicrographs showing clay minerals along the surface of stylolite. (A) Clustered goethites partially filled microfractures, leaving some still empty segments of microfractures visible; (B) Halite with various sizes fills the interranular pores; (C) Both kaolinite and quartz fills interganular pores along stylolites; (D) Quartz partly fills the intergranular pores along a stylolite.

Fig. 10 Histograms showing frequency distributions of porosity (A) and permeability

(B) of carbonate cap rock samples with bedding-parallel stylolites (N=28); (C) Cross-plot of porosity versus permeability of carbonate cap rock samples containing bedding-parallel stylolites; (D) Sealing capacity comparison (defined as average cover coefficient) of carbonate cap rocks that contains four stylolite types (rectangular layer, seismogram pinning, suture & sharp peak and simple wave-like stylolite) of the Lower-Middle Ordovician Yingshan Formation in the Tarim Basin.

Fig. 11 High-pressure mercury intrusion porosimetry (HPMIP) analysis curves to obtain pore throat radii distribution and permeability contribution value of selected representative carbonate cap rocks containing four types of stylolites. (A) and (B) Sample P8 with rectangular layer stylolite, φ=1.4%, K=0.002 mD; (C) and (D) Sample P5 with seismogram pinning stylolite, φ=1.4%, K=0.192 mD; (E) and (F) Sample A9 with suture & sharp peak stylolite from the, φ=1.1%, K=0.002 mD; (G) and (H) Sample P14 with simple wave-like stylolite, φ=0.7%, K=0.002 mD. Samples (A), (C) and (G) are from the Dabantage outcrop and Sample (E) is from the Penglaiba outcrop.

Fig. 12 Quantity of four types of stylolites and their corresponding lithologic types of carbonate cap rocks of the Yingshan Formation in the Tarim Basin. (A) Rectangular layer type; (B) Seismogram pinning type; (C) Suture & sharp peak type; (D) Simple wave-like type.

Fig. 13 Cross-plot of porosity vs. permeability in relation to four stylolite types of carbonate cap rock samples of the Yingshan Formation in the Tarim Basin. (A)

Rectangular layer type; (B) Seismogram pinning type; (C) Suture & sharp peak type; (D) Simple wave-like type.

Fig. 14 Comparison of lithologic types and sealing behaviors in four types of stylolite-dominated carbonate cap rocks in the Tarim Basin. (A) Rectangular layer stylolites are most abundant in grainstone and have three sealing segments (good, moderate and poor); (B) Seismogram pinning stylolites are most abundant in grainstone and present two sealing segments (moderate and poor); (C) Suture & sharp peak stylolites are most abundant in wackestone to packstone and show two sealing segments (good and moderate); (D) Simple wave-like stylolites are most abundant in mudstone and wackestone to packstone and have a good sealing performance.

Table 1 Statistical analysis of the proportion of lithologic types for the stylolitized carbonate cap rocks from outcrop sections (n=46) and drill wells (n=79) of the Ordovician Yingshan Formation in the Tarim Basin.

Lithologic type	Outcrop samples (n=46)	Well samples (n=79)	Outcrop and well samples (n=125)
Mudstone	15.2%	38%	29.6%
Wackestone to packstone	43.5%	38%	40%
Grainstone	34.8%	20.2%	25.6%
Dolomitic limestone	6.5%	3.8%	4.8%

Table 2 The proportion of each stylolite type with respect to the total stylolites and cover coefficient (*CC*) of sixteen carbonate cap rocks.

Sample ID	Lithologic type	Proportion of this stylolite type with respect to the total stylolites				*CC* (%)
		Rectangular layer	Seismogram pinning	Suture & sharp peak	Simple wave-like	
PLB-A19	Mudstone	0	0.45	0	0.55	3.9
PLB-A21	Mudstone	0	0.86	0	0.14	4.26
PLB-A22	Mudstone	0	0	0	1	4.71
DBTG-P3	Grainstone	0	0	0.35	0.65	4.23
DBTG-P6	Dolomitic limestone	0	1	0	0	4.58
DBTG-P7	Dolomitic limestone	0	0	0	1	4.89
DBTG-P10	Grainstone	0.12	0	0.56	0.32	5.40
DBTG-P14	Dolomitic limestone	0	0	0	1	4.54
YJK-L2	Grainstone	0	1	0	0	4.56
YJK-L6	Mudstone	0	0	0	1	4.81
YJK-L7	Mudstone	0	0	0	1	4.13
SNC-E15	Grainstone	0	1	0	0	4.25
SNC-E21	Grainstone	0	0	0.7	0.3	4.14
SNC-E25	Grainstone	0	0	0	1	4.59
SNC-E26	Grainstone	0	0	1	0	4.28
SNC-E28	Mudstone	0.35	0	0.65	0	4.17

Table 3 Relationship between lithologic type, petrophysical property, pore structure and sealing capacity in the four types of stylolites.

Stylolite type	Lithologic type	Relationship between porosity vs. permeability	Pore structure feature			Sequence of sealing capacity
			Pore size range (μm)	Dominate pores	Sequence of threshold pressure	
Rectangular layer	Peloidal/intraclastic grainstone	Obvious negative	0.0063–1.6	Transitional pore-II	2	2
Seismogram pinning	Peloidal/intraclastic grainstone bioclastic/peloidal wackestone	No correlation	0.0063–63	Macropores-I	4	4
Suture & sharp peak	Bioclastic/peloidal wackestone peloidal/intraclastic packstone	Relatively good	0.0063–1.6	Mesopores-I and mesopores-II	3	3
Simple wave-like	Mudstone	Obvious positive	0.0063–0.025	Transitional pore-II and micropores	1	1

Table 4 Relationship between stylolite morphology and sealing potential for carbonate cap rocks in the Tarim Basin.

Stylolite type	Segments of sealing potential	Typical feature in the stylolite	Acting role for the sealing capacity
Rectangular layer	Good	Layer remnants are pervasively distributed, and sealing materials are collected at the bottom and top of stylolite teeth tips	Effective fluid flow barriers
	Moderate	Some calcite veins are distributed parallel to the flanks of stylolite and a large amount of pyrobitumen and pyrite is present at their teeth.	Barriers for fluid flow
	Poor	Neither calcite cements nor pyrobitumen are visible at the teeth flanks.	New fluid pathways and cause local leaking
Seismogram pinning	Moderate	Sealing materials precipitate in the pronounced high-amplitude stylolite teeth and medium surface	Inhibiting fluid flow across the stylolite
	Poor	Insoluble material is only collected in the median surface. The offset, dissolution holes and lack of insoluble residues along the stylolite flanks.	Local efficient barriers for fluid flow
Suture & sharp peak	Good	Abundant insoluble clay-rich residuals and surrounding precipitation of cements are collected and accumulated.	Efficient fluid flow barriers
	Moderate	Local precipitation of cements along the pressure-solution interfaces, and insoluble residues are offset by spikes.	An obstacle for regional fluid flow
Simple wave-like	Good	Thick residues along the low-amplitude stylolite, and insoluble pyrobitumen residues completely fill the stylolite interfaces	Very continuous and efficient barriers

Figure 1

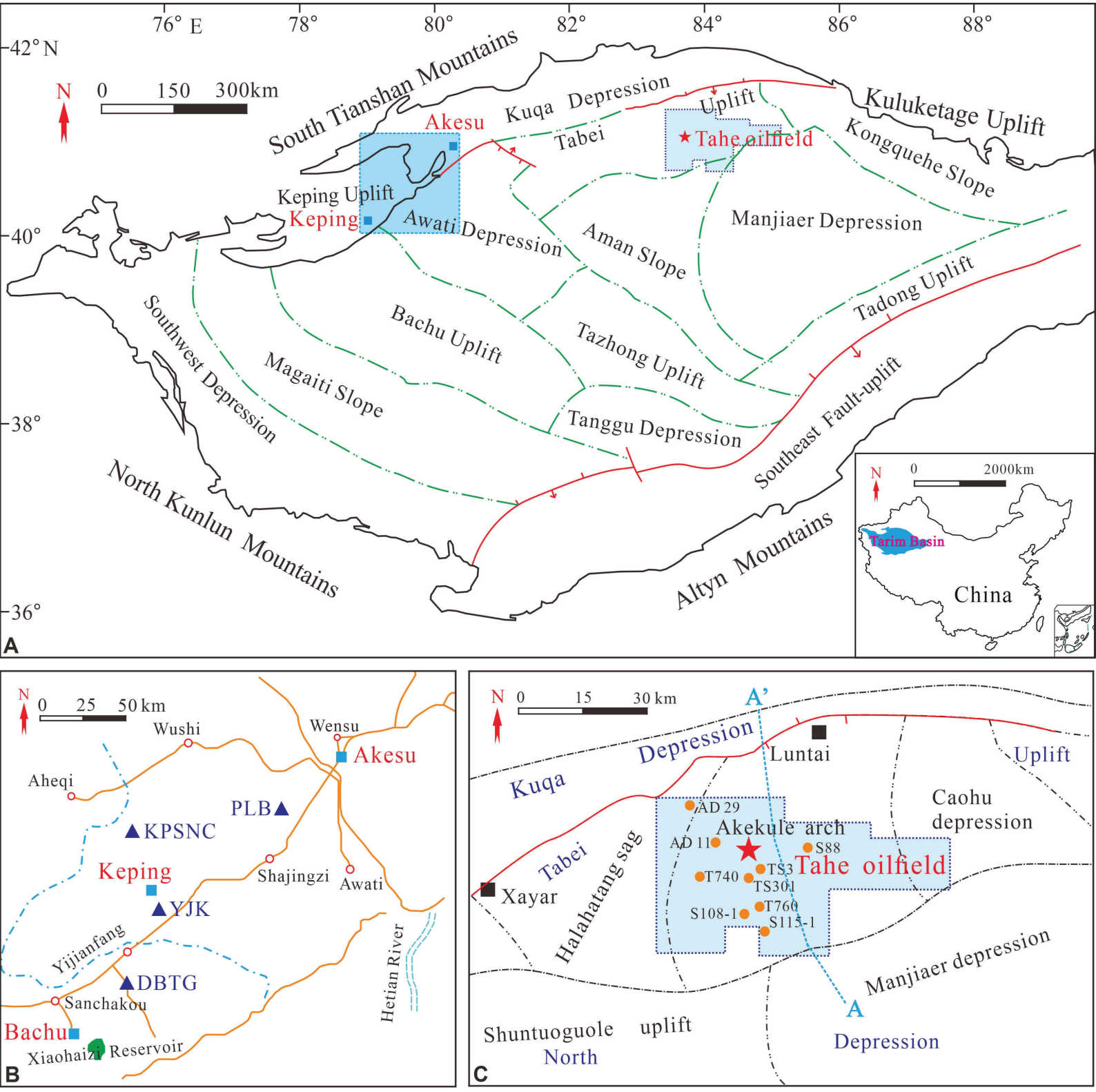

Basin boundary | Structural boundary | Fault | Road | Administative boundary | City | Outcrop | Well | First unit boundary | Second unit boundary

Figure 2

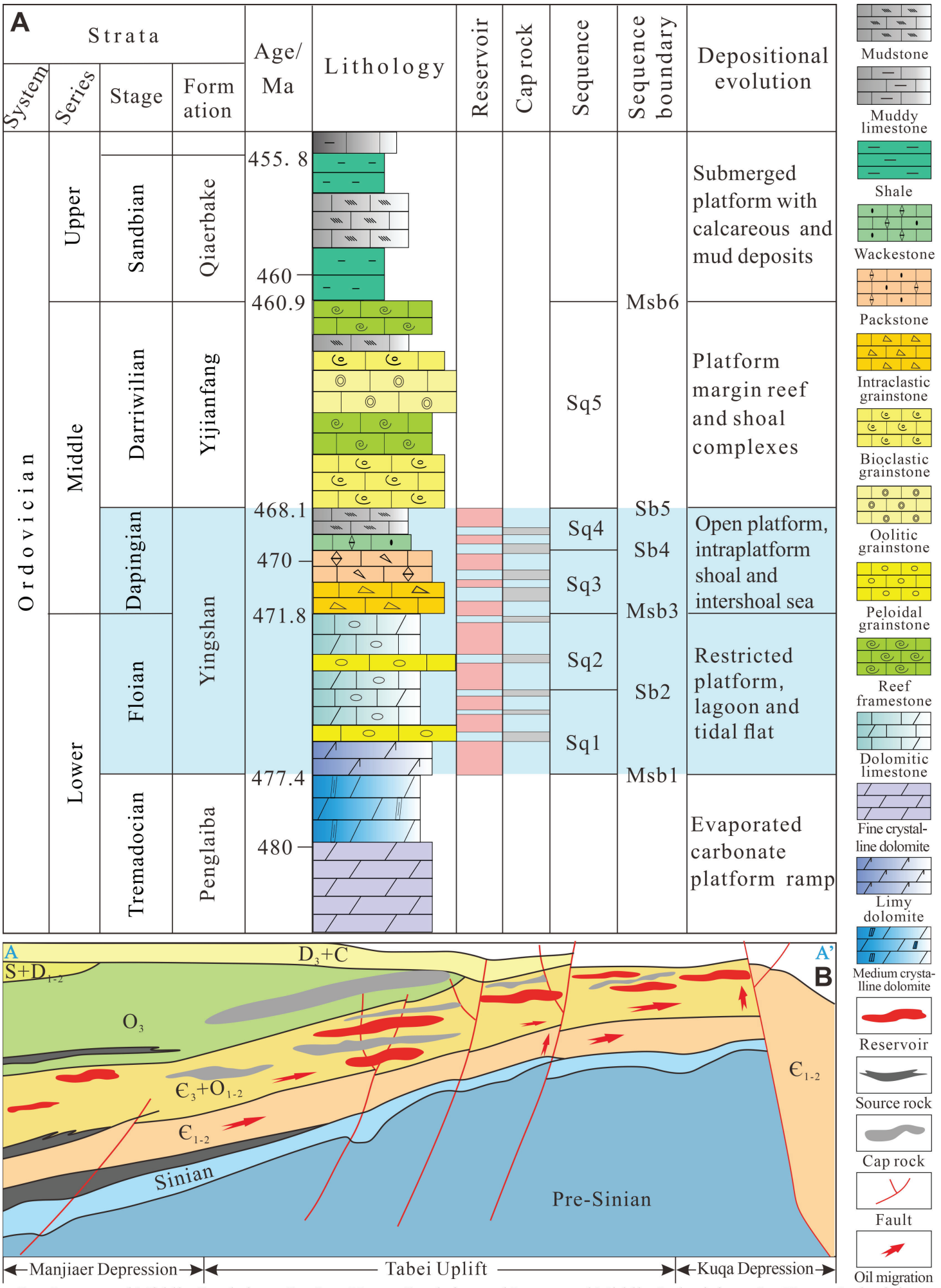

$\in_{1-2}$=Lower and Middle Cambrian; $\in_3+O_{1-2}$=Upper Cambrian and Lower and Middle Ordovician; O_3=Upper Ordovician; $S+D_{1-2}$=Silurian and Lower and Middle Devonian; D_3+C=Upper Devonian and Carboniferous.

Figure 3

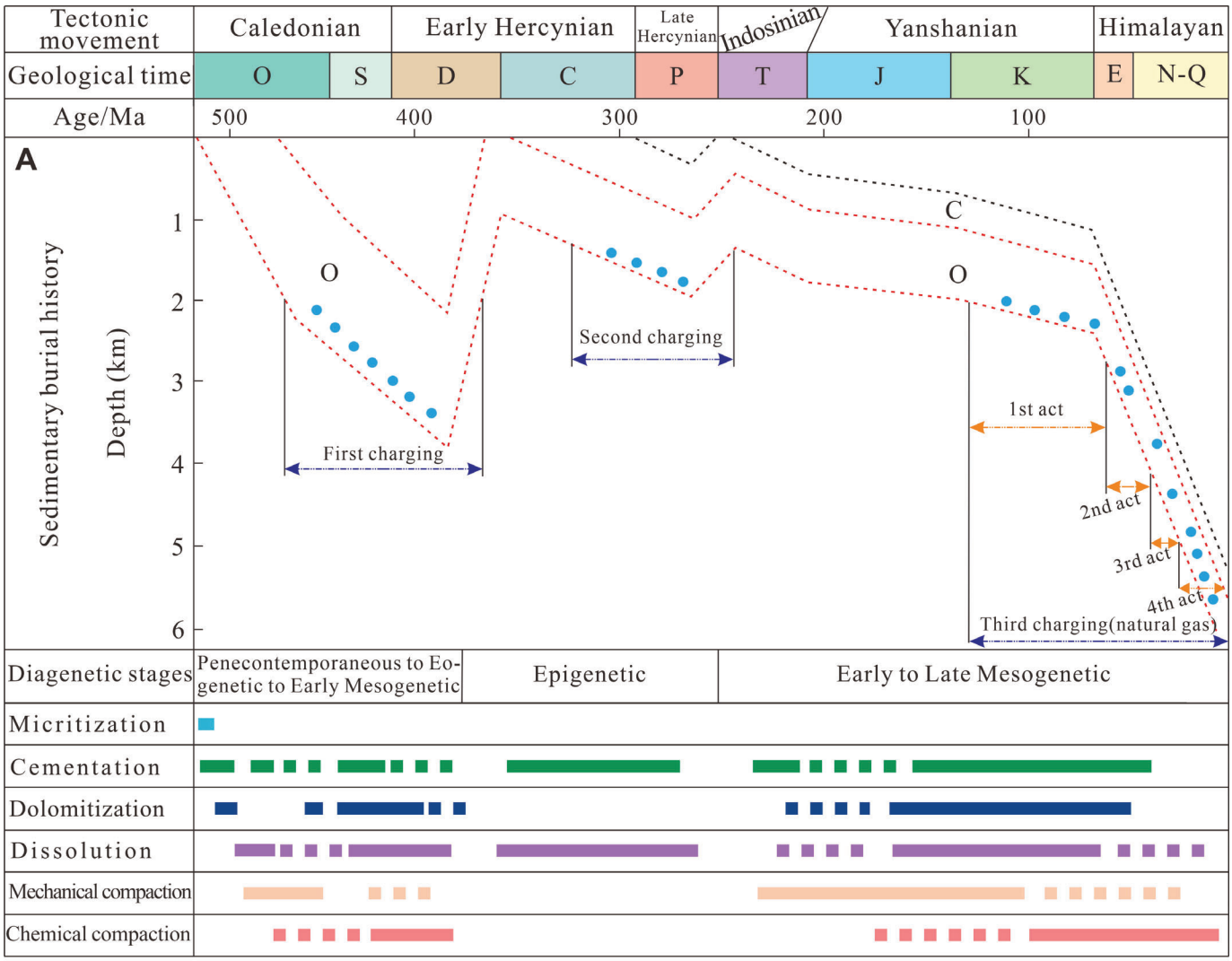
Tectonic movement
Caledonian
Early Hercynian
Late Hercynian
Indosinian
Yanshanian
Himalayan
Geological time
O
S
D
C
P
T
J
K
E
N-Q
Age/Ma
500
400
300
200
100
A
Sedimentary burial history
Depth (km)
1
2
3
4
5
6
O
C
O
First charging
Second charging
1st act
2nd act
3rd act
4th act
Third charging(natural gas)
Diagenetic stages
Penecontemporaneous to Eo-genetic to Early Mesogenetic
Epigenetic
Early to Late Mesogenetic
Micritization
Cementation
Dolomitization
Dissolution
Mechanical compaction
Chemical compaction

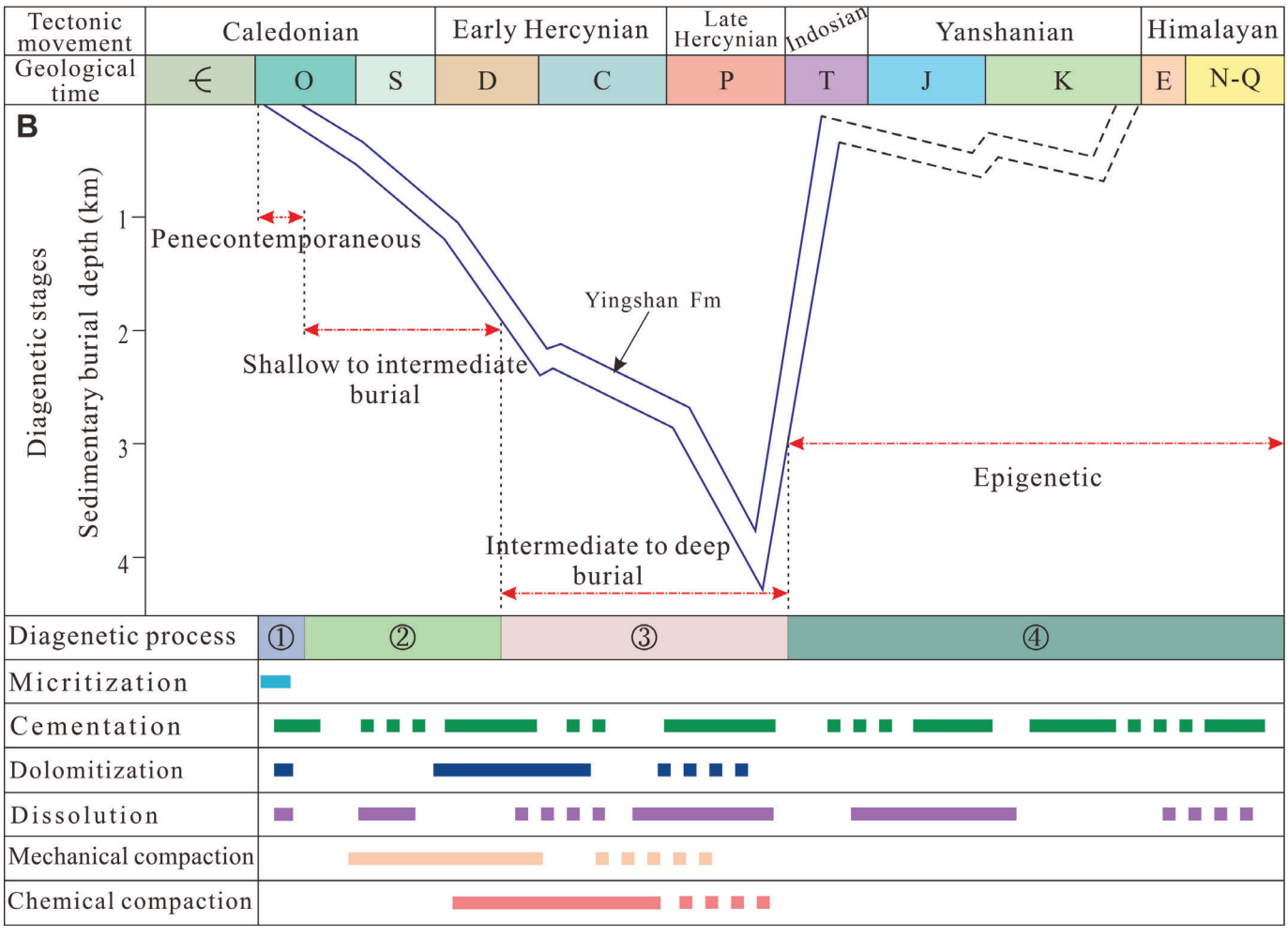
Tectonic movement
Caledonian
Early Hercynian
Late Hercynian
Indosian
Yanshanian
Himalayan
Geological time
∈
O
S
D
C
P
T
J
K
E
N-Q
B
Diagenetic stages
Sedimentary burial depth (km)
1
2
3
4
Penecontemporaneous
Shallow to intermediate burial
Yingshan Fm
Intermediate to deep burial
Epigenetic
Diagenetic process
①
②
③
④
Micritization
Cementation
Dolomitization
Dissolution
Mechanical compaction
Chemical compaction

Figure 4

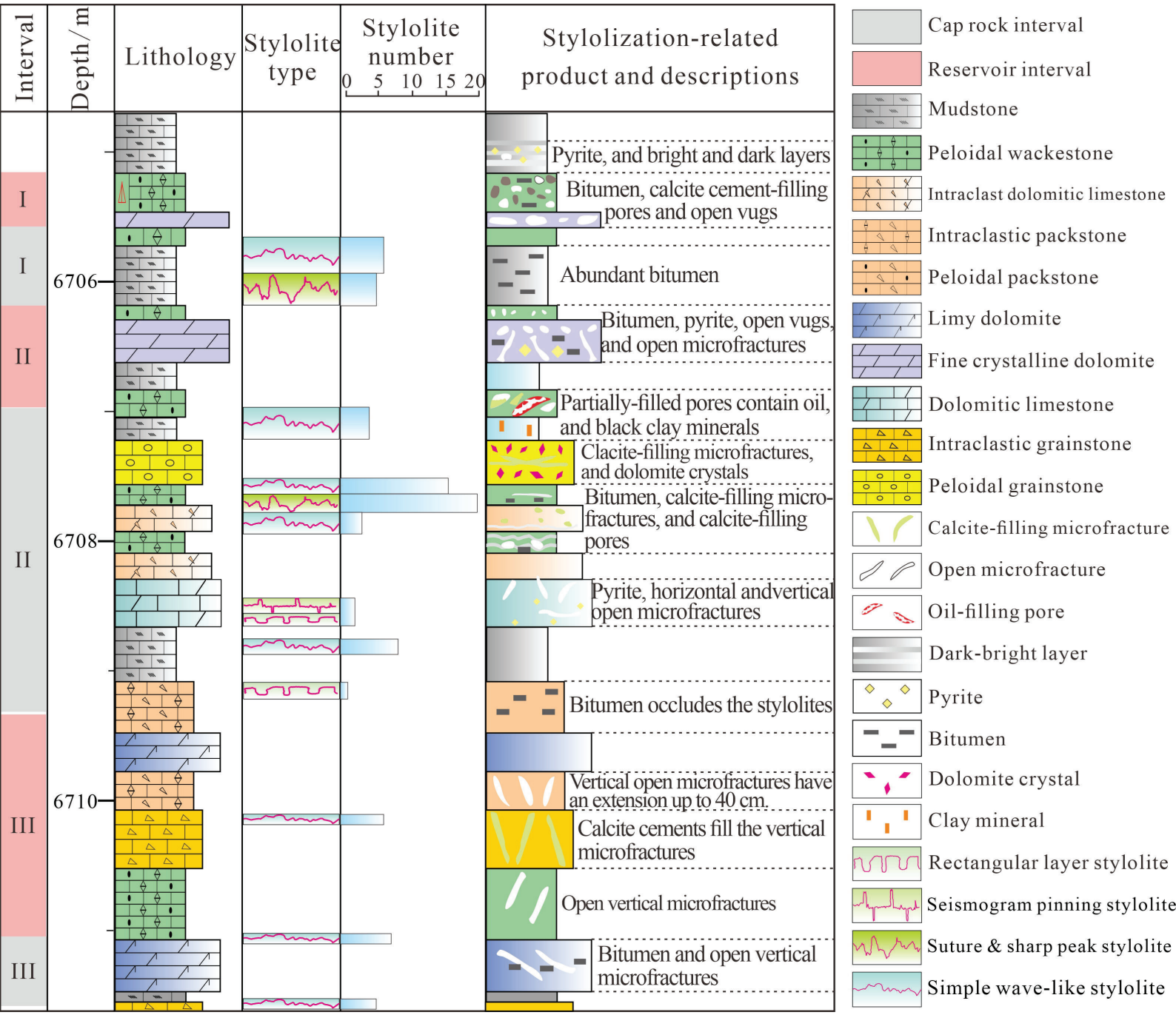
Interval
Depth/m
Lithology
Stylolite type
Stylolite number
0 5 10 15 20
Stylolization-related product and descriptions
I
I
II
II
III
III
6706
6708
6710
Pyrite, and bright and dark layers
Bitumen, calcite cement-filling pores and open vugs
Abundant bitumen
Bitumen, pyrite, open vugs, and open microfractures
Partially-filled pores contain oil, and black clay minerals
Clacite-filling microfractures, and dolomite crystals
Bitumen, calcite-filling micro-fractures, and calcite-filling pores
Pyrite, horizontal andvertical open microfractures
Bitumen occludes the stylolites
Vertical open microfractures have an extension up to 40 cm.
Calcite cements fill the vertical microfractures
Open vertical microfractures
Bitumen and open vertical microfractures
Cap rock interval
Reservoir interval
Mudstone
Peloidal wackestone
Intraclast dolomitic limestone
Intraclastic packstone
Peloidal packstone
Limy dolomite
Fine crystalline dolomite
Dolomitic limestone
Intraclastic grainstone
Peloidal grainstone
Calcite-filling microfracture
Open microfracture
Oil-filling pore
Dark-bright layer
Pyrite
Bitumen
Dolomite crystal
Clay mineral
Rectangular layer stylolite
Seismogram pinning stylolite
Suture & sharp peak stylolite
Simple wave-like stylolite

Figure 5

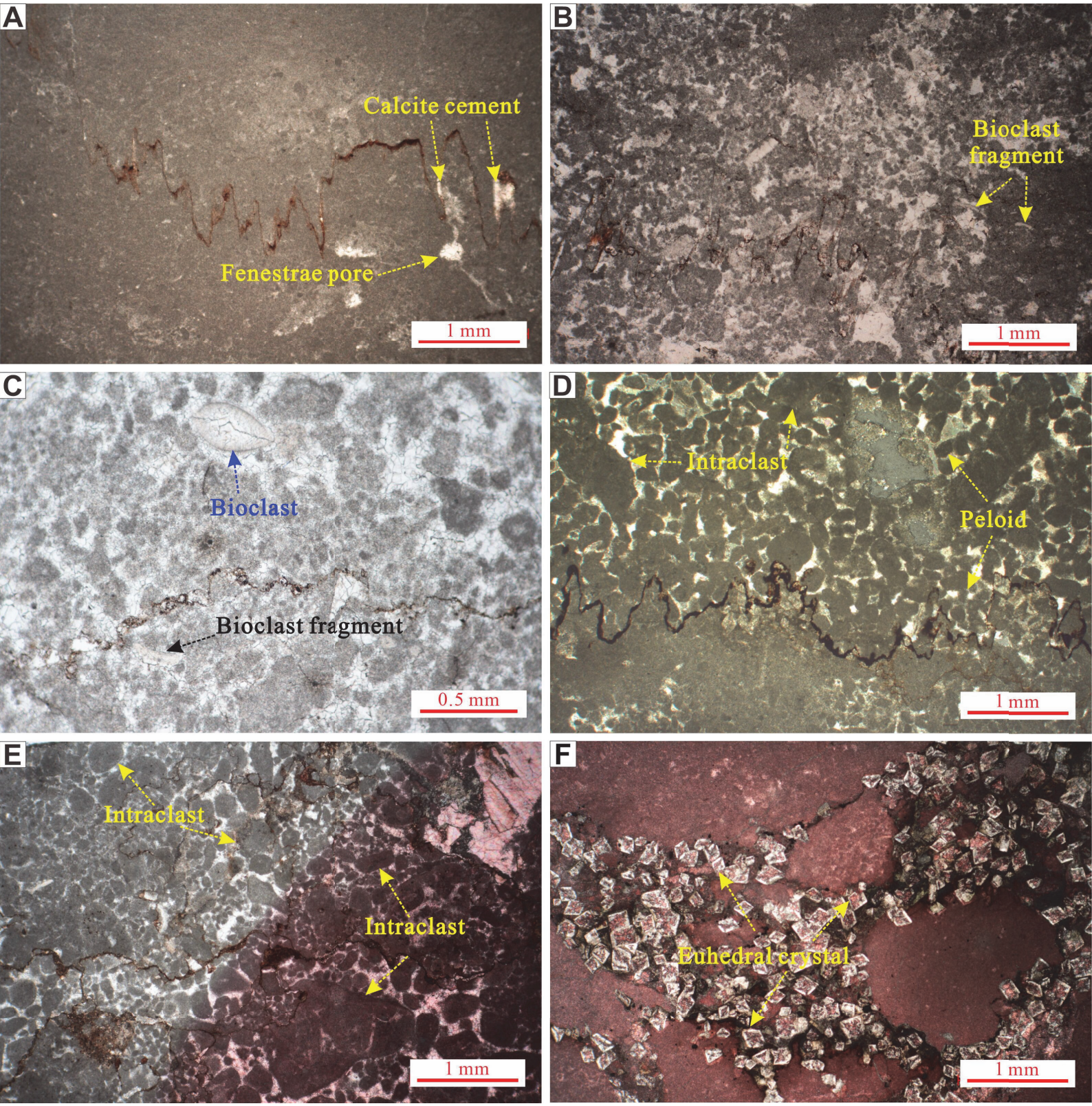
A
Calcite cement
Fenestrae pore
1 mm
B
Bioclast fragment
1 mm
C
Bioclast
Bioclast fragment
0.5 mm
D
Intraclast
Peloid
1 mm
E
Intraclast
Intraclast
1 mm
F
Euhedral crystal
1 mm

Figure 6

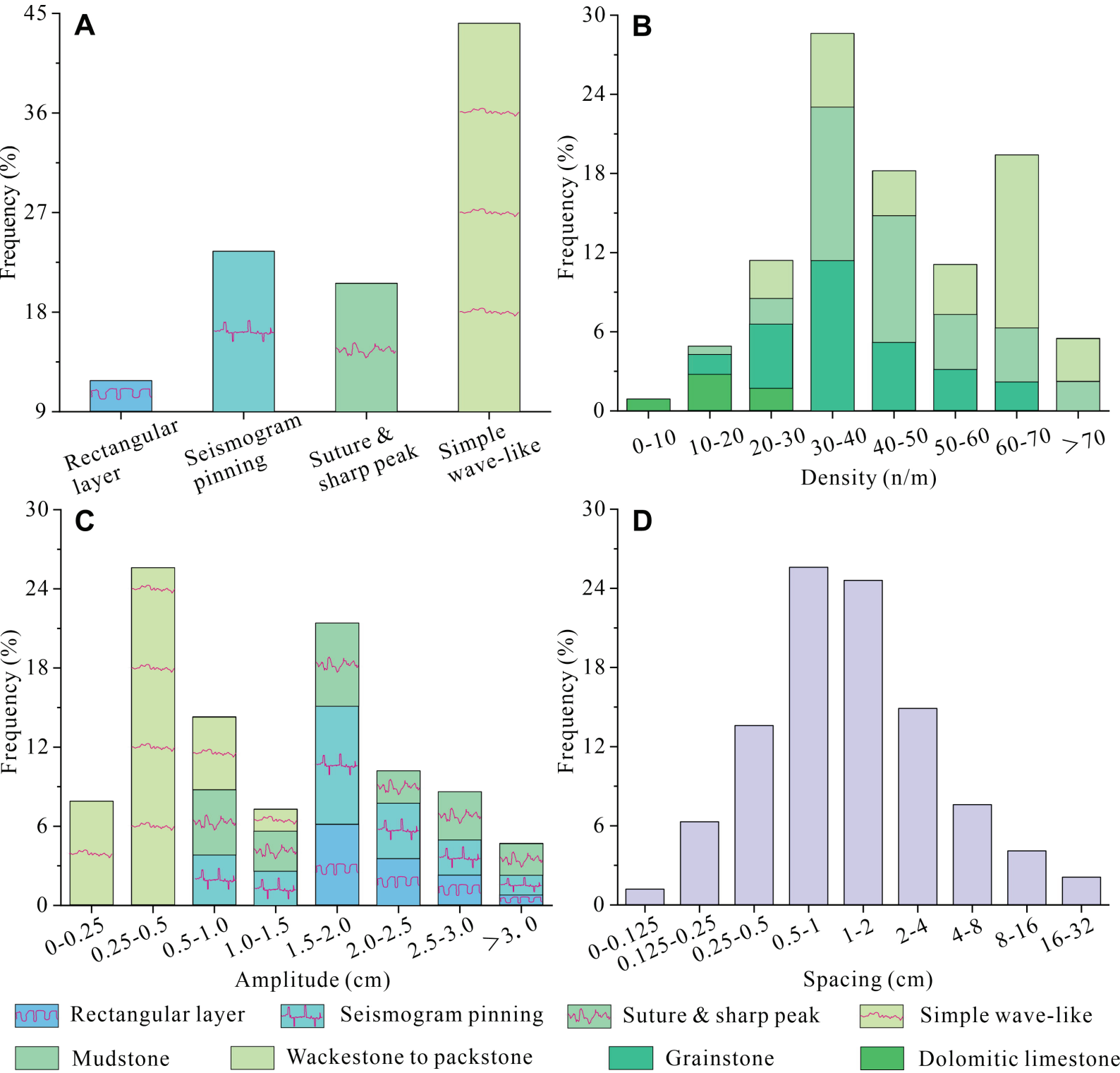
A
Frequency (%)
45
36
27
18
9
Rectangular layer
Seismogram pinning
Suture & sharp peak
Simple wave-like
B
Frequency (%)
30
24
18
12
6
0
0-10
10-20
20-30
30-40
40-50
50-60
60-70
>70
Density (n/m)
C
Frequency (%)
30
24
18
12
6
0
0-0.25
0.25-0.5
0.5-1.0
1.0-1.5
1.5-2.0
2.0-2.5
2.5-3.0
>3.0
Amplitude (cm)
D
Frequency (%)
30
24
18
12
6
0
0-0.125
0.125-0.25
0.25-0.5
0.5-1
1-2
2-4
4-8
8-16
16-32
Spacing (cm)
Rectangular layer
Seismogram pinning
Suture & sharp peak
Simple wave-like
Mudstone
Wackestone to packstone
Grainstone
Dolomitic limestone

Figure 7

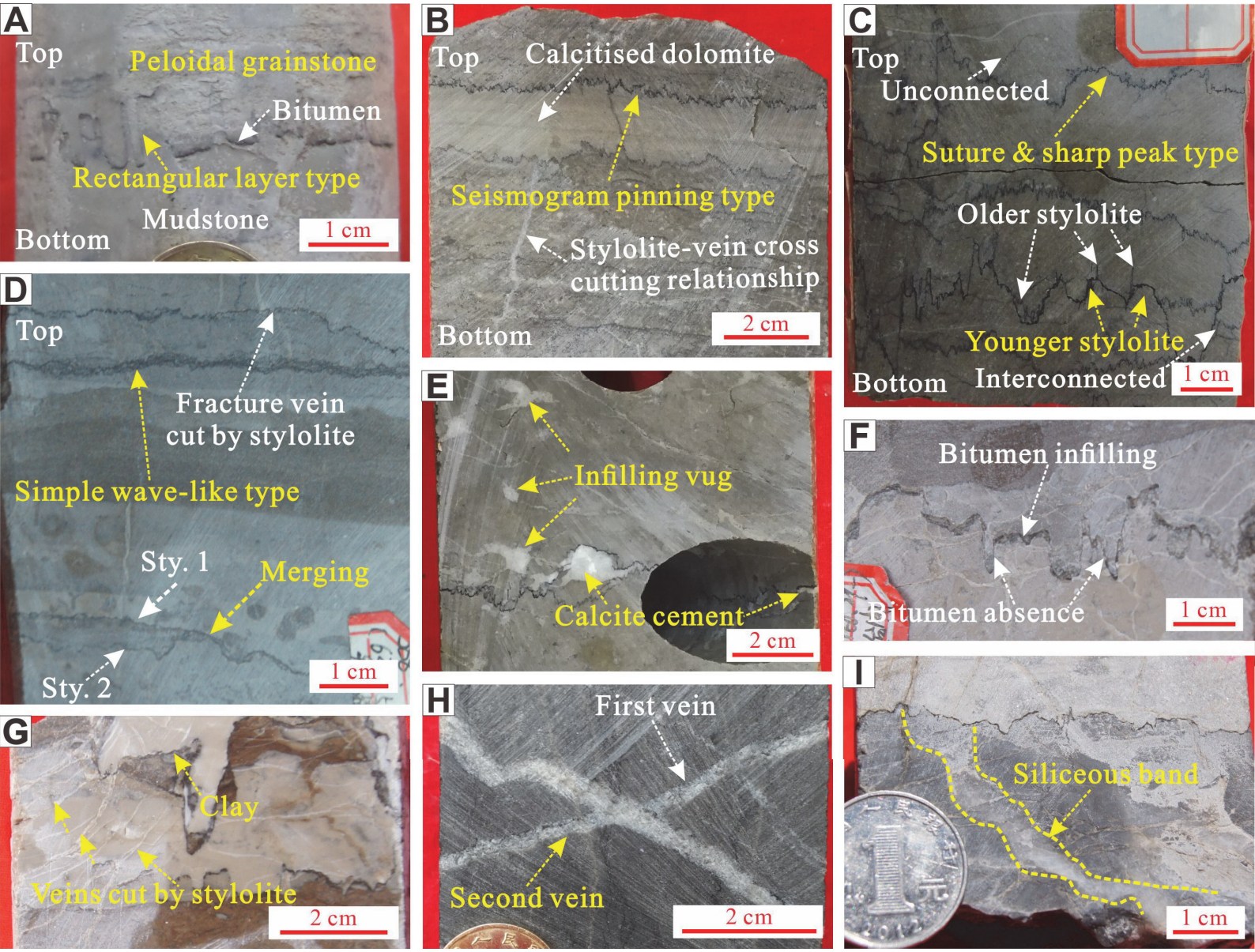
A
Top
Peloidal grainstone
Bitumen
Rectangular layer type
Mudstone
Bottom
1 cm
B
Top
Calcitised dolomite
Seismogram pinning type
Stylolite-vein cross cutting relationship
Bottom
2 cm
C
Top
Unconnected
Suture & sharp peak type
Older stylolite
Younger stylolite
Bottom
Interconnected
1 cm
D
Top
Fracture vein cut by stylolite
Simple wave-like type
Sty. 1
Merging
Sty. 2
1 cm
E
Infilling vug
Calcite cement
2 cm
F
Bitumen infilling
Bitumen absence
1 cm
G
Clay
Veins cut by stylolite
2 cm
H
First vein
Second vein
2 cm
I
Siliceous band
1 cm

Figure 8

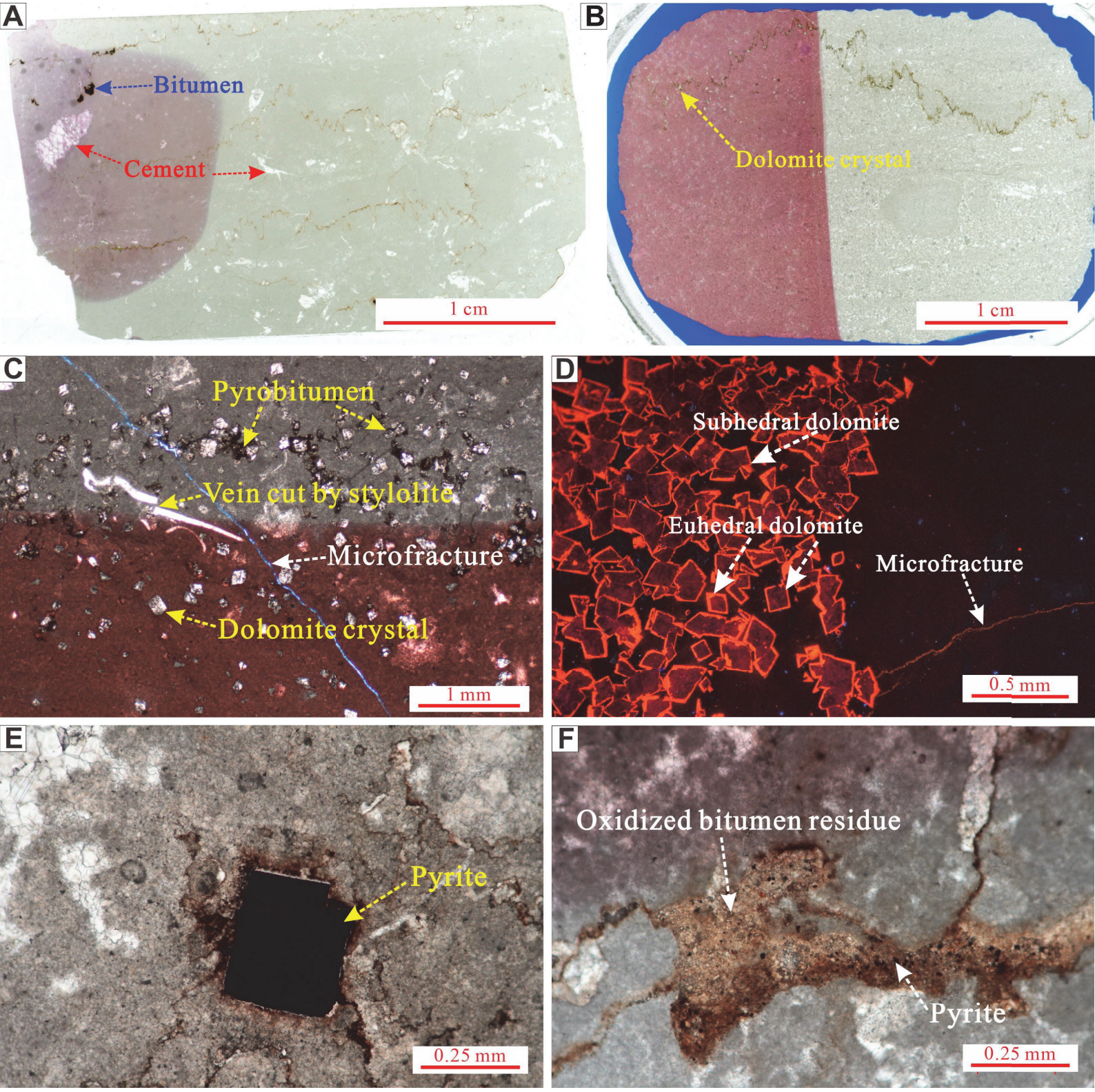
A
Bitumen
Cement
1 cm
B
Dolomite crystal
1 cm
C
Pyrobitumen
Vein cut by stylolite
Microfracture
Dolomite crystal
1 mm
D
Subhedral dolomite
Euhedral dolomite
Microfracture
0.5 mm
E
Pyrite
0.25 mm
F
Oxidized bitumen residue
Pyrite
0.25 mm

Figure 9

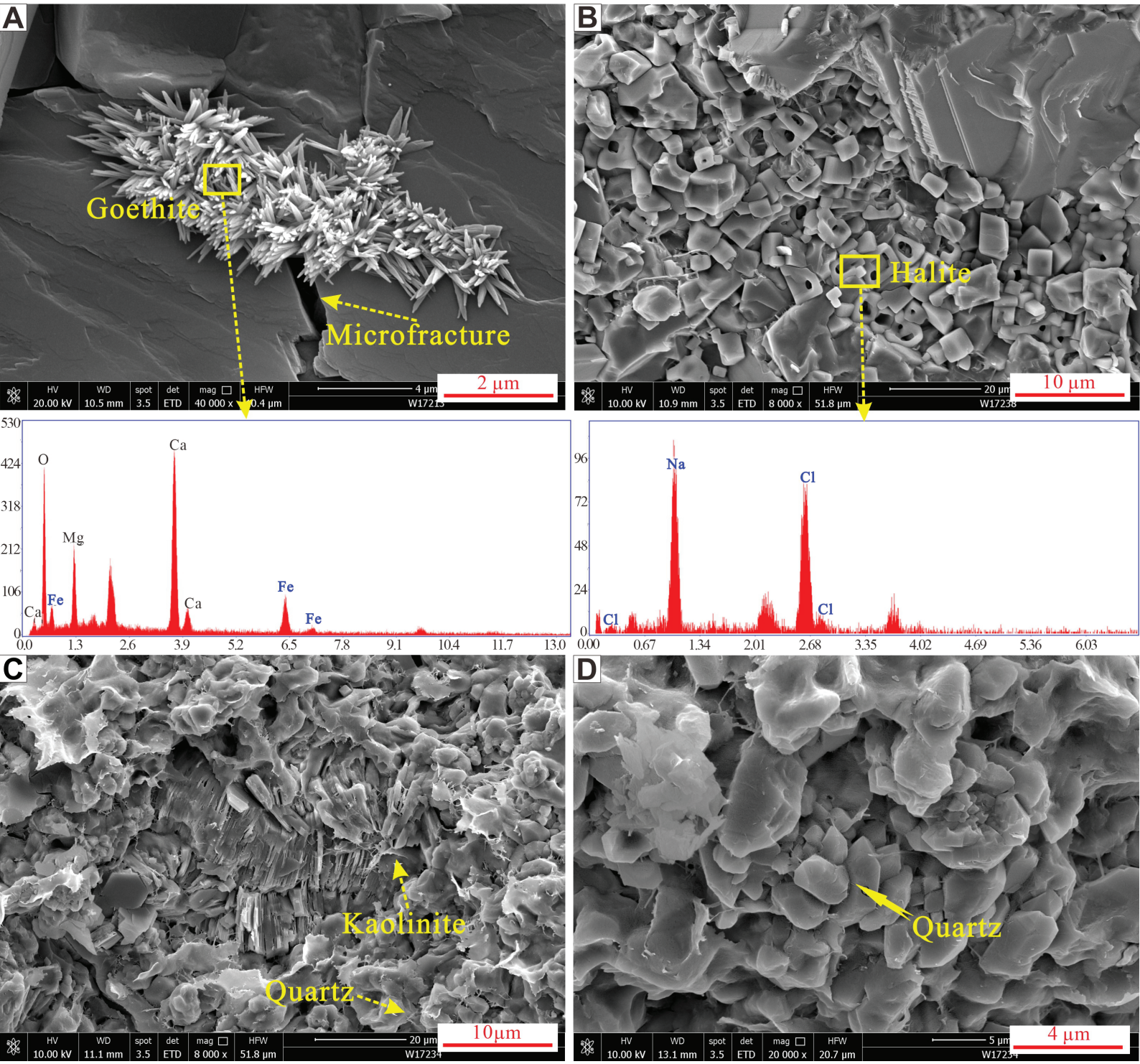
A
Goethite
Microfracture
2 µm
B
Halite
10 µm
O
Ca
Mg
Fe
Ca
Ca
Fe
Fe
Na
Cl
Cl
Cl
C
Kaolinite
Quartz
10µm
D
Quartz
4 µm

Figure 10

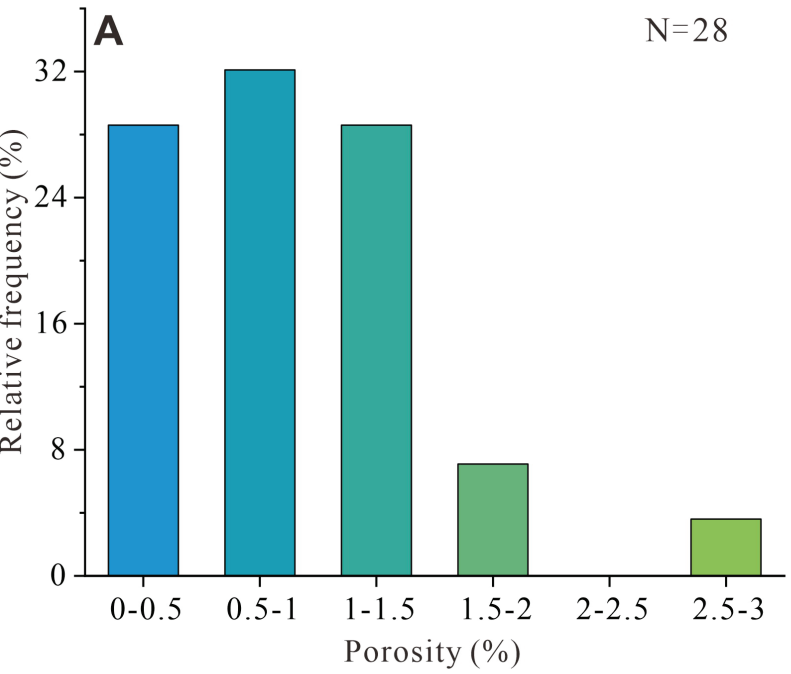
A
N=28
Relative frequency (%)
32
24
16
8
0
0-0.5
0.5-1
1-1.5
1.5-2
2-2.5
2.5-3
Porosity (%)

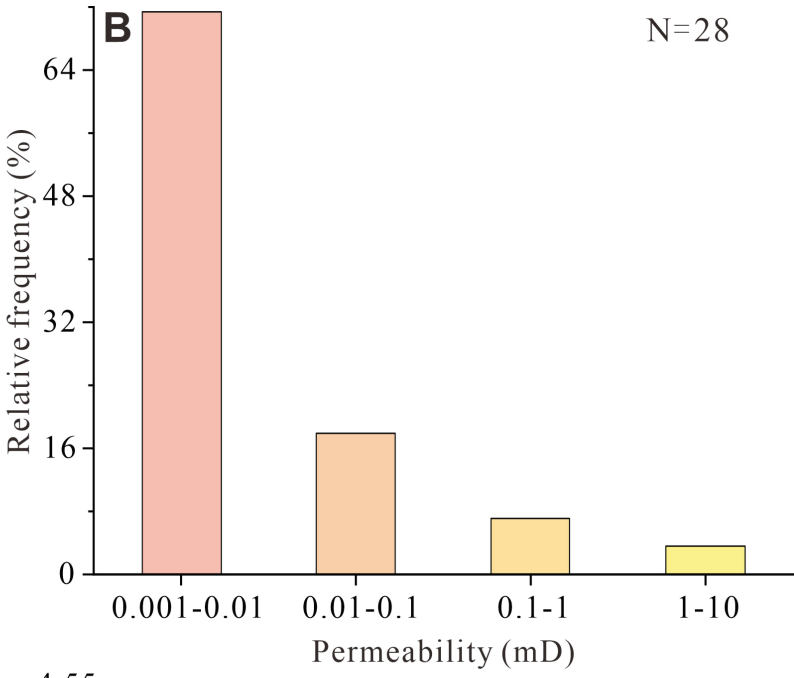
B
N=28
Relative frequency (%)
64
48
32
16
0
0.001-0.01
0.01-0.1
0.1-1
1-10
Permeability (mD)

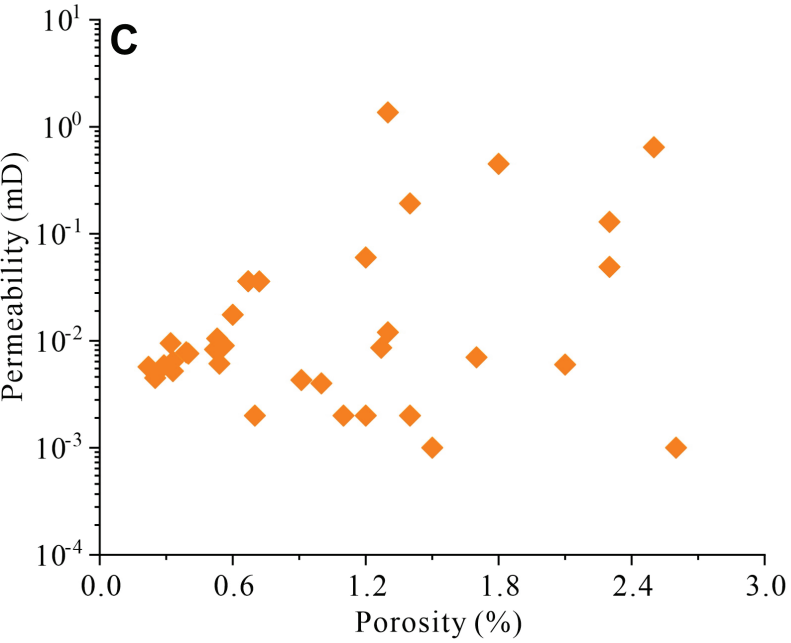
C
Permeability (mD)
10^1
10^0
10^-1
10^-2
10^-3
10^-4
0.0
0.6
1.2
1.8
2.4
3.0
Porosity (%)

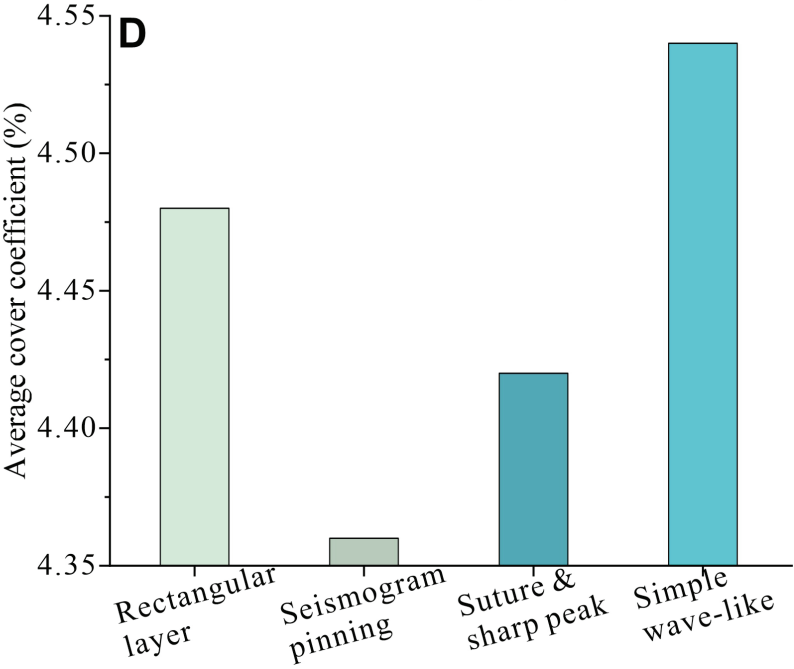
D
Average cover coefficient (%)
4.55
4.50
4.45
4.40
4.35
Rectangular layer
Seismogram pinning
Suture & sharp peak
Simple wave-like

Figure 11

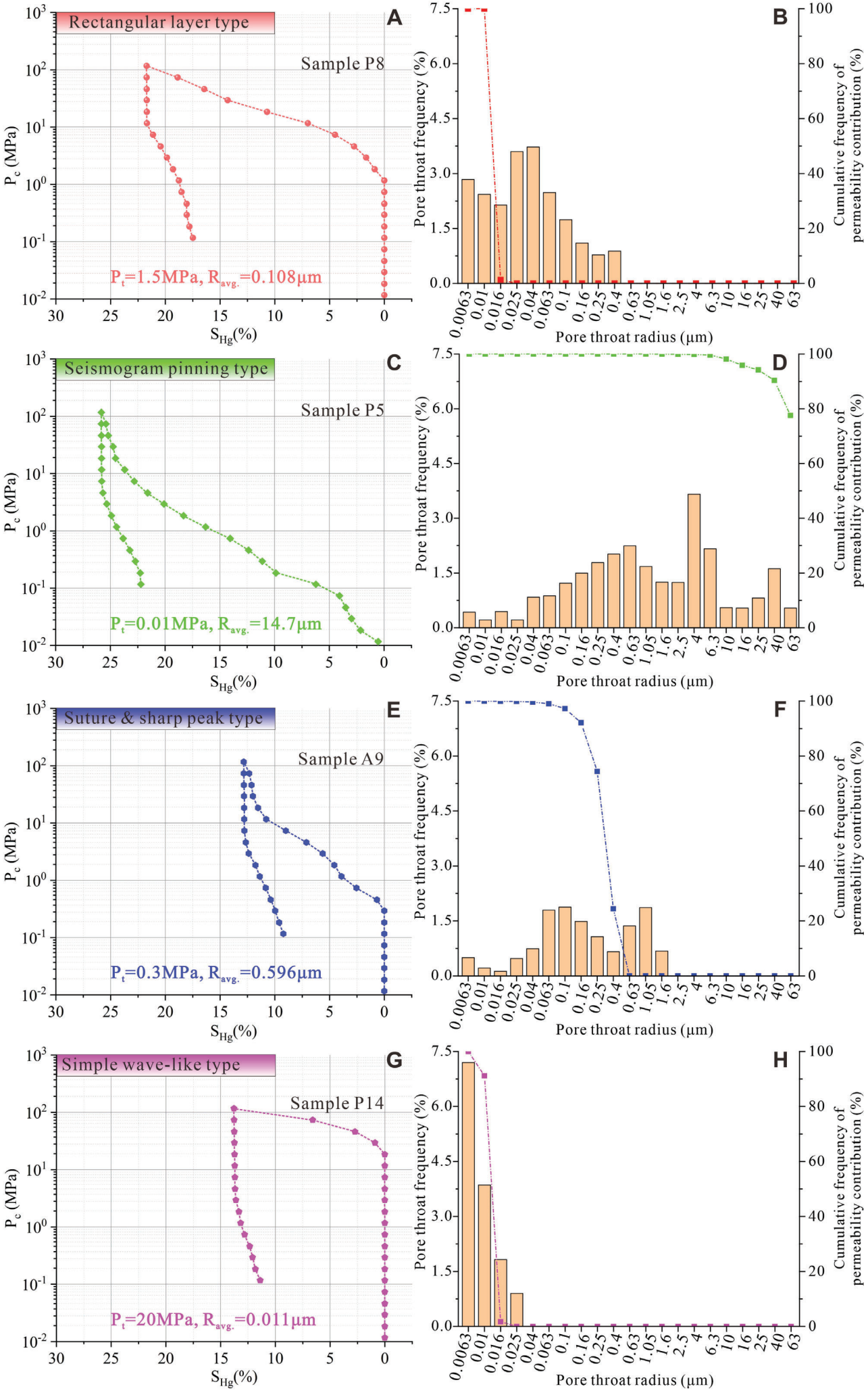
Rectangular layer type
A
Sample P8
P_t=1.5MPa, $R_{avg.}$=0.108μm
B
Seismogram pinning type
C
Sample P5
P_t=0.01MPa, $R_{avg.}$=14.7μm
D
Suture & sharp peak type
E
Sample A9
P_t=0.3MPa, $R_{avg.}$=0.596μm
F
Simple wave-like type
G
Sample P14
P_t=20MPa, $R_{avg.}$=0.011μm
H
P_c (MPa)
S_{Hg}(%)
Pore throat frequency (%)
Cumulative frequency of permeability contribution (%)
Pore throat radius (μm)
0.0063
0.01
0.016
0.025
0.04
0.063
0.1
0.16
0.25
0.4
0.63
1.05
1.6
2.5
4
6.3
10
16
25
40
63

Figure 12

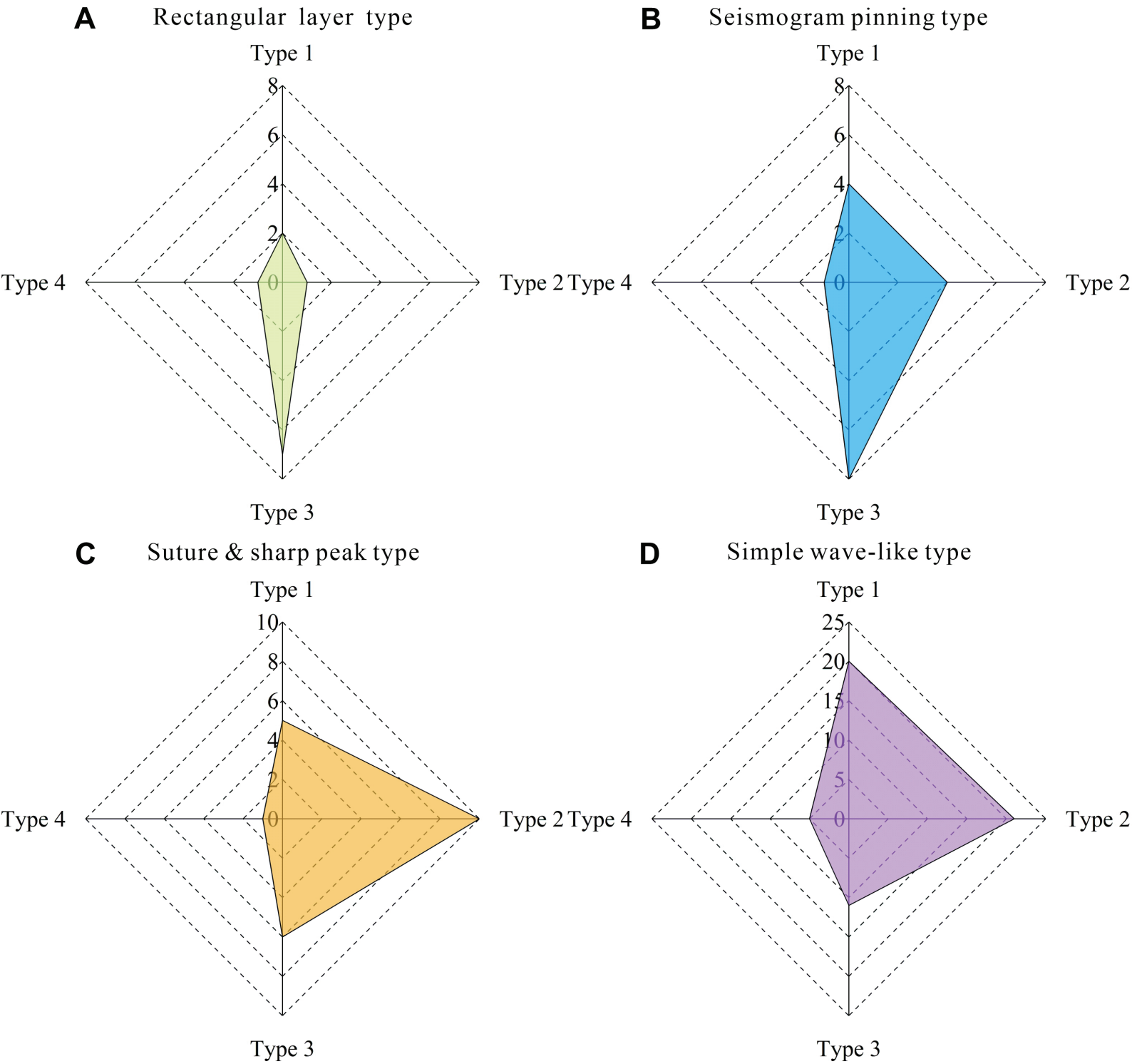

Type 1: Mudstone Type 2: Wackestone to packstone Type 3: Grainstone Type 4: Dolomitic limestone

Figure 13

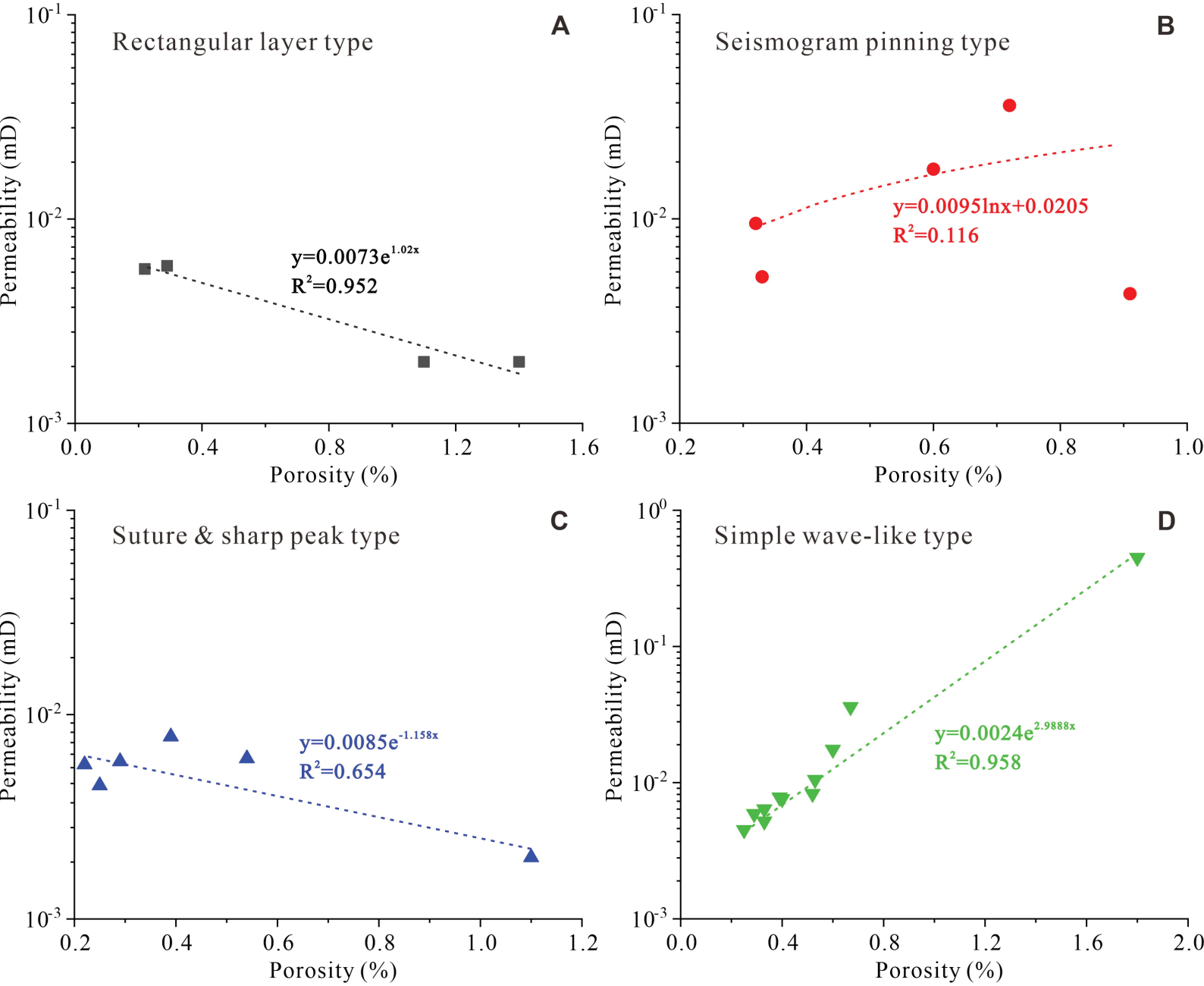
A
Rectangular layer type
y=0.0073e^1.02x
R²=0.952
Permeability (mD)
Porosity (%)
B
Seismogram pinning type
y=0.0095lnx+0.0205
R²=0.116
Permeability (mD)
Porosity (%)
C
Suture & sharp peak type
y=0.0085e^-1.158x
R²=0.654
Permeability (mD)
Porosity (%)
D
Simple wave-like type
y=0.0024e^2.9888x
R²=0.958
Permeability (mD)
Porosity (%)

Figure 14

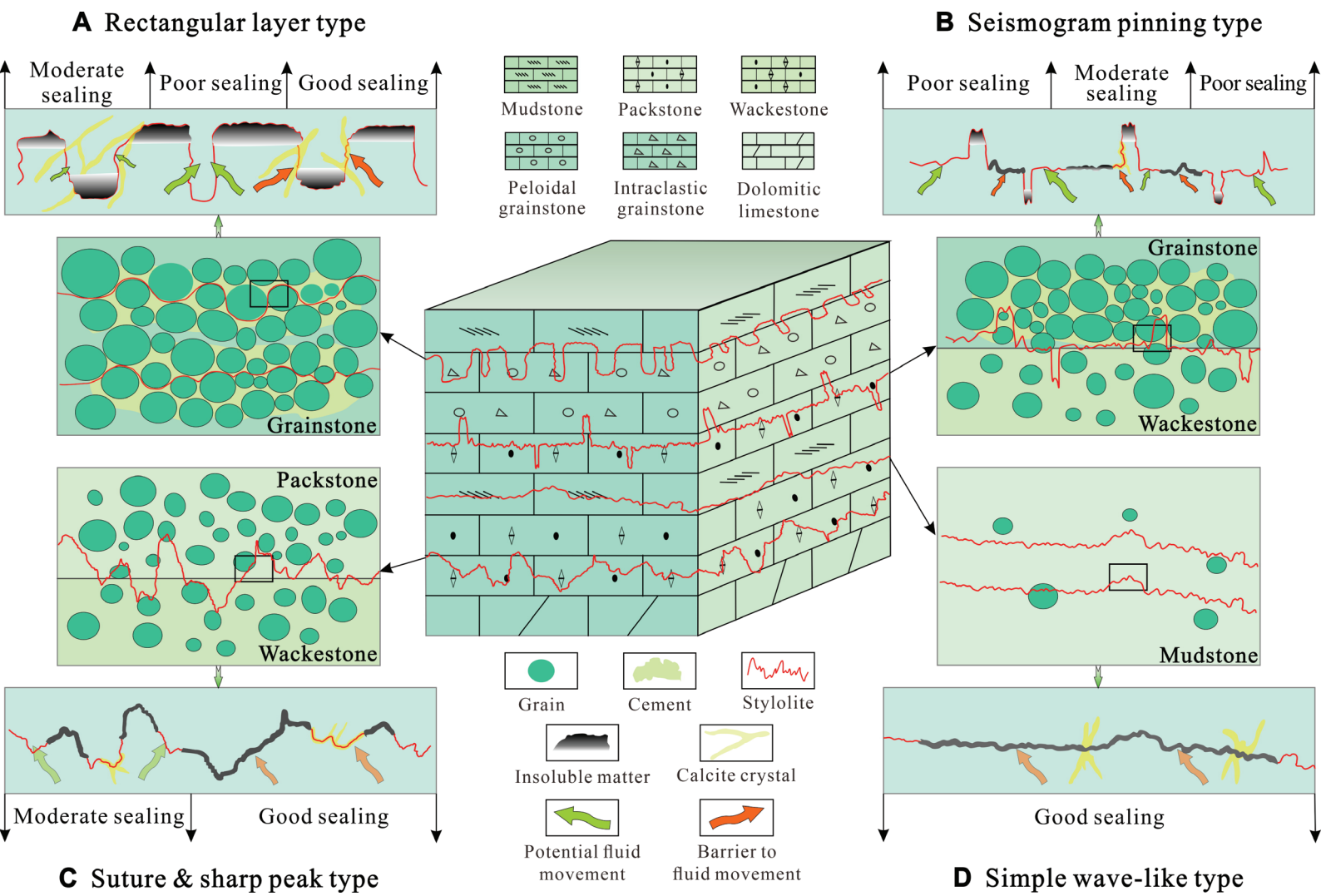
A Rectangular layer type
Moderate sealing
Poor sealing
Good sealing
Grainstone
Packstone
Wackestone
Moderate sealing
Good sealing
C Suture & sharp peak type
B Seismogram pinning type
Poor sealing
Moderate sealing
Poor sealing
Grainstone
Wackestone
Mudstone
Good sealing
D Simple wave-like type
Mudstone
Packstone
Wackestone
Peloidal grainstone
Intraclastic grainstone
Dolomitic limestone
Grain
Cement
Stylolite
Insoluble matter
Calcite crystal
Potential fluid movement
Barrier to fluid movement